Materials Today Bio 26 (2024) 101059

Contents lists available at ScienceDirect

Materials Today Bio

journal homepage: www.journals.elsevier.com/materials-today-bio

Biocompatible adipose extracellular matrix and reduced graphene oxide nanocomposite for tissue engineering applications

Kest Verstappen [a], Alexey Klymov [a], Mónica Cicuéndez [b], Daniela M. da Silva [c], Nathalie Barroca [c], Francisco-Javier Fernández-San-Argimiro [d], Iratxe Madarieta [d], Laura Casarrubios [e], María José Feito [e], Rosalía Diez-Orejas [f], Rita Ferreira [g], Sander C.G. Leeuwenburgh [a], María Teresa Portolés [e,h], Paula A.A.P. Marques [c], X. Frank Walboomers [a,*]

[a] *Department of Dentistry-Regenerative Biomaterials, Research Institute for Medical Innovation, Radboud University Medical Center, 6525 EX, Nijmegen, the Netherlands*
[b] *Department of Chemistry in Pharmaceutical Sciences, Faculty of Pharmacy, Complutense University of Madrid, Health Research Institute of the Hospital Clínico San Carlos (IdISSC), 28040, Madrid, Spain*
[c] *Centre for Mechanical Technology and Automation (TEMA), Intelligent Systems Associate Laboratory (LASI), Department of Mechanical Engineering, University of Aveiro, 3810-193, Aveiro, Portugal*
[d] *TECNALIA, Basque Research and Technology Alliance (BRTA), E20009, Donostia-San Sebastian, Spain*
[e] *Department of Biochemistry and Molecular Biology, Faculty of Chemistry, Complutense University of Madrid, Health Research Institute of the Hospital Clínico San Carlos (IdISSC), 28040, Madrid, Spain*
[f] *Department of Microbiology and Parasitology, Faculty of Pharmacy, Complutense University of Madrid, Health Research Institute of the Hospital Clínico San Carlos (IdISSC), 28040, Madrid, Spain*
[g] *Associated Laboratory for Green Chemistry of the Network of Chemistry and Technology (LAQV-REQUIMTE), Department of Chemistry, University of Aveiro, 3810-193, Aveiro, Portugal*
[h] *Biomedical Research Networking Center in Bioengineering, Biomaterials and Nanomedicine (CIBER-BBN), Institute of Health Carlos III (ISCIII), 28040, Madrid, Spain*

ARTICLE INFO

Keywords:
Cytotoxicity
Extracellular matrix
Graphene
Nanocomposite
Macrophages
Foreign body response

ABSTRACT

Despite the immense need for effective treatment of spinal cord injury (SCI), no successful repair strategy has yet been clinically implemented. Multifunctional biomaterials, based on porcine adipose tissue-derived extracellular matrix (adECM) and reduced graphene oxide (rGO), were recently shown to stimulate *in vitro* neural stem cell growth and differentiation. Nevertheless, their functional performance in clinically more relevant *in vivo* conditions remains largely unknown. Before clinical application of these adECM-rGO nanocomposites can be considered, a rigorous assessment of the cytotoxicity and biocompatibility of these biomaterials is required. For instance, xenogeneic adECM scaffolds could still harbour potential immunogenicity following decellularization. In addition, the toxicity of rGO has been studied before, yet often in experimental settings that do not bear relevance to regenerative medicine. Therefore, the present study aimed to assess both the *in vitro* as well as *in vivo* safety of adECM and adECM-rGO scaffolds. First, pulmonary, renal and hepato-cytotoxicity as well as macrophage polarization studies showed that scaffolds were benign *in vitro*. Then, a laminectomy was performed at the 10th thoracic vertebra, and scaffolds were implanted directly contacting the spinal cord. For a total duration of 6 weeks, animal welfare was not negatively affected. Histological analysis demonstrated the degradation of adECM scaffolds and subsequent tissue remodeling. Graphene-based scaffolds showed a very limited fibrous encapsulation, while rGO sheets were engulfed by foreign body giant cells. Furthermore, all scaffolds were infiltrated by macrophages, which were largely polarized towards a pro-regenerative phenotype. Lastly, organ-specific histopathology and biochemical analysis of blood did not reveal any adverse effects. In summary, both adECM and adECM-rGO implants were biocompatible upon laminectomy while establishing a pro-regenerative microenvironment, which justifies further research on their therapeutic potential for treatment of SCI.

* Corresponding author.
E-mail addresses: Kest.Verstappen@radboudumc.nl (K. Verstappen), Alexey.Klymov@radboudumc.nl (A. Klymov), mcicuendez@ucm.es (M. Cicuéndez), danielas@ua.pt (D.M. da Silva), nbarroca@ua.pt (N. Barroca), xabier.fernandez@tecnalia.com (F.-J. Fernández-San-Argimiro), iratxe.madarieta@tecnalia.com (I. Madarieta), laura.casarrubios.molina@gmail.com (L. Casarrubios), mjfeito@ucm.es (M.J. Feito), rosaliad@farm.ucm.es (R. Diez-Orejas), ritaferreira@ua.pt (R. Ferreira), Sander.Leeuwenburgh@radboudumc.nl (S.C.G. Leeuwenburgh), portoles@quim.ucm.es (M.T. Portolés), paulam@ua.pt (P.A.A.P. Marques), frank.walboomers@radboudumc.nl (X.F. Walboomers).

https://doi.org/10.1016/j.mtbio.2024.101059
Received 17 January 2024; Received in revised form 30 March 2024; Accepted 13 April 2024
Available online 17 April 2024

1. Introduction

Spinal cord injury (SCI) is a particularly devastating neurological condition that results in the partial or complete loss of motor and sensory function below the injury site. The pathophysiology of SCI is complex, involving primary and secondary injury mechanisms. As a direct consequence of the initial mechanical insult, disruption of tissue integrity initiates a secondary injury cascade including hemorrhage, inflammation, ischemia and neuronal and glial cell death. The later stages of SCI are hallmarked by the formation of cystic cavities and the glial scar, both potent inhibitors of regeneration, causing permanent neurological deficits [1]. Due to the intricate organization of the spinal cord and the multifaceted nature of SCI, no successful therapeutic strategy has yet been clinically implemented [2]. Current experimental research therefore aims to counteract multiple aspects of SCI, for instance by pursuing neural re-innervation and immunomodulation [3,4]. Multifunctional biomaterials, including nanocomposites [5,6], that are capable of targeting various aspects of SCI, will likely be more effective as a therapeutic strategy for this complex injury [7].

Naturally derived materials, such as decellularized extracellular matrix (ECM), offer a variety of advantages for applications in neural regenerative medicine [8]. These include inherent bioactivity, a high degree of native ligand distribution, excellent biocompatibility and biodegradability, and the ability to initiate neovascularization [9–11]. Adipose decellularized ECM (adECM) especially preserves almost all of the native ECM proteins, including basement membrane proteins, that are indispensable for tissue regeneration [12]. Within the context of neural regeneration, controlled degradation of adECM would allow for gradual replacement of lost tissue. However, since these naturally derived matrices are highly biodegradable, further functionalization of the scaffold is still required to match the biodegradation rate of these matrices with the rate of tissue regeneration *in situ*. This can be realized by harnessing the reinforcing effects of reduced graphene oxide (rGO) [13]. The incorporation of rGO nanosheets into biomimetic constructs is especially attractive, as this has the potential to increase conductivity and offer various opportunities to stimulate electrically active neuronal cells [14,15]. In terms of electrical properties at a local scale, these rGO flakes exhibit electrical conductivity of about 10.1 $S.m^{-1}$ [16], which was pointed out as a regulating factor for enhanced cell-ECM interactions and cell-cell communication [17]. The role of rGO for neural tissue engineering goes far beyond granting electroconductivity to the scaffold. For instance, rGO scaffolds supported the formation of highly interconnected neural cultures *in vitro*, rich in dendrites, axons and synaptic connections, and facilitated the formation of myelinated axons and mature blood vessels *in vivo*, indicative of the promising regenerative features of rGO [18,19].

Distinctively from these previous approaches wherein the strategy relied on rGO as a standalone, our group has developed a novel organic-inorganic nanocomposite – adECM-rGO – where the rGO serves as the building block supporting the adECM biochemical environment [20]. When probed between top and bottom, these composites were not electrically conductive but rather presented differences in relation to the rGO-free scaffolds in terms of local surface potential. Specifically, adECM-rGO composites had a higher surface potential and a more pronounced gradient of surface potential across the scaffold, stemming from the spatial distribution of the adECM and rGO, their interaction and interface [20]. Importantly, the adECM-rGO composites induced an increased differentiation of neural stem cells into neurons, as compared to the rGO-free scaffolds [20]. However, prior to applying graphene-based materials (GBMs), such as adECM-rGO composites, in preclinical SCI models, it is imperative to carefully validate the materials' safety. Nonetheless, compared to the numerous early-stage proof-of-concept studies found in literature, preclinical validation studies are typically considered less novel and hence fall into an interest gap [21]. In fact, preclinical safety validation is essential in the commercial and clinical translation of promising therapies. It is generally recognized that the success of biomaterial-mediated therapeutics, such as our adECM-rGO nanocomposite, critically depends on the material's cytotoxicity and the foreign body reaction (FBR), including immune cell infiltration, tissue remodeling, and fibrous encapsulation [22,23]. The xenogeneic porcine origin of the supportive adECM could still impose a risk for immunogenicity due to inefficient decellularization or antigen removal methods [24]. The toxicity of GBMs is governed by a variety of physicochemical properties, such as size [25,26], surface chemistry [27], or degree of reduction [28]. For instance, transcutaneous and intraperitoneal injection of rGO demonstrated an attenuated FBR and less chronic inflammation compared to similarly dosed graphene oxide (GO), even though the reduced form was more rapidly infiltrated by immune cells [29]. Next to that, the experimental model used along with administration routes [29], dose [27] and frequency [30] all influence the materials' biocompatibility [13]. Importantly, the majority of safety investigations involves an injection of GBMs, e.g. intravenous (*iv*), often resulting in organ-specific biodistribution, accumulation and subsequent inflammation [31]. These investigations, however, are often not relevant for applications in regenerative medicine. Here, GBMs would typically be injected or implanted at specific target sites for extended periods of time, which might result in completely distinct biocompatibility profiles [29]. Hence, a rigorous assessment of cytotoxicity, FBR, and biodistribution is warranted to confirm the biocompatibility of implanted GBMs, to pave the way for its clinical translation.

In this context, the present study focused on the *in vitro* and *in vivo* safety validation of adECM and adECM-rGO scaffolds, in an experimental setting that is highly relevant to neural tissue engineering strategies following SCI. Regarding *in vitro* testing, scaffold cytotoxicity using multiple relevant cell types as well as macrophage polarization towards M1 and M2 phenotypes were evaluated. For *in vivo* experimentation, a laminectomy at the 10th thoracic vertebra was created in rats. Both adECM and adECM-rGO scaffolds were subsequently implanted to ensure direct contact with the spinal cord. Potential adverse effects on animal welfare were monitored using a post-operative care protocol to detect any signs of pain or distress, respiratory failure, and dehydration, among others. Histological analysis was performed to investigate the host-material interplay, including cell infiltration and fibrous encapsulation. Finally, plasma analysis as well as histopathological assessment of relevant organs, such as the lungs and liver, were performed to rule out any systemic or organ-specific toxicity. Overall, our study provides critical insight into the safety of xenogeneic adECM-rGO nanocomposites, which contributes to the advancement of these materials as a novel therapeutic strategy to treat SCI.

2. Materials and methods

2.1. Fabrication of adECM and adECM-rGO solid foams

A commercial dispersion of GO nanosheets (0.4 wt%) in water (Graphenea, San Sebastián, Spain) was firstly dialyzed against distilled water for 7 days to remove chemical impurities and freeze-dried to avoid nanosheet agglomeration. The reduction of GO was thereafter performed by thermal annealing at 200 °C for 30 min. The reduction degree was characterized by X-ray photoelectron spectroscopy (XPS) using the Phoibos 150 electron analyzer (SPECS, Berlin, Germany), in an ultra-high vacuum system (pressure of 2×10^{-8} Pa) using a normal emission take-off angle and 20 eV pass-energy and a monochromatic Al Kα (1486.74 eV) X-ray source. Porcine adipose tissue-derived ECM (adECM; Tecnalia, San Sebastián, Spain) was obtained in a similar manner as reported before [12]. Remnant DNA was analyzed using the Quant-iT PicoGreen dsDNA assay (Thermo Fisher Scientific, Waltham, MA, USA) according to the manufacturer's instructions. Concerning adECM, 37.0 ± 1.8 ng/mg remnant DNA was detected, well below the established decellularization criteria of 50 ng DNA/mg dry weight. Total protein content was measured using the Pierce BCA protein assay kit (Thermo Fisher Scientific) and collagen content was assessed using the

Sircol assay kit (Biocolor, Carrickfergus, UK), and both were similar to previously published reports [12].

Scaffolds of adECM and adECM-rGO composites (50/50 wt%) were fabricated by solid-liquid phase separation as previously described by our group [20]. This concentration of rGO, i.e. 50 wt %, induced an increased differentiation of neural stem cells into neurons and was therefore selected for the present study [20]. In brief, rGO was thoroughly dispersed in 0.1 M of acetic acid by sonication. The adECM was then added and dissolved for 48 h at a concentration of 10 mg mL^{-1}. Circular dichroism (CD) spectroscopy was performed to assess protein conformational changes of adECM in acidic conditions. Data were recorded with a J-815 CD spectrometer (JASCO, Easton, MD, USA) equipped with a PTC-423S/15 Peltier accessory (JASCO) at 10 °C, using a wavelength between 260 and 190 nm with increments of 0.5 nm and an equilibrium time of 2 min. Crosslinking was induced by adding the following coupling agents: 1-Ethyl-3-(3-dimethylaminopropyl)carbodiimide) (EDC) and N-hydroxysuccinimide (NHS) at a concentration of EDC of 3.3 μmol per mg of adECM and an EDC:NHS molar ratio of 1. After 2h, the solutions were cast on a 48 well plate using 450 μL of solution per well, frozen at −20 °C overnight and freeze-dried for 2 days. Following freeze-drying, scaffolds were thoroughly washed with distilled water to remove any residual reagents and subproducts, and freeze-dried again.

2.2. Physico-chemical characterization of adECM and adECM-rGO solid foams

Morphological evaluation was performed by scanning electron microscopy (SEM; Hitachi TM4000 plus, Tokyo, Japan), at an accelerating voltage of 15 kV. Additionally, X-ray microtomography (μCT; SkyScan 1275, Bruker, Billerica, MA, USA) was performed at the following conditions: 25 kV, 160 μA with a rotation step of 0.2°, exposure time of 250 ms and nominal resolution of 6.0 μm. Reconstruction of μCT projections was done in NRecon software (Bruker). The morphometric analysis (porosity and pore size distribution) was conducted in CTan software (Bruker). The macroscopic mechanical properties of scaffolds were determined using an electromechanical material tester (MMT-101NV-10, Shimadzu, Kyoto, Japan), by compressing the swollen scaffolds in phosphate buffered saline (PBS) at a rate of 5 mm min^{-1}. Eight samples were used for each scaffold type and compressive Young's modulus was calculated from the linear regime of the respective stress-strain curves. Mechanical properties of both scaffolds were measured by oscillatory shear rheology using a parallel-plate geometry (20 mm diameter, steel, with a gap of 1 mm) of a HR 20 rheometer (TA Instruments, New Castle, DE, USA). Stress amplitude sweeps were performed at a constance frequency of 0.1 Hz to fix the amplitude parameter for each sample and to ensure subsequent data were collected in the linear viscoelastic regime. All measurements were made in duplicate at room temperature (RT) in constant deformation control mode over a frequency range from 0.1 to 100 rad s^{-1}. The viscoelastic behaviour of the adECM and adECM-rGO scaffolds was measured at the selected amplitude of 0.02 Pa and scanning the frequency (0.01–10 rad s^{-1}) at this constant amplitude. Water uptake capacity was analyzed by immersing the scaffolds (five samples) in PBS for several periods of time (1, 2, 4, 8, 24 and 48 h) at 37 °C. Swelling ratio was calculated according to eq. (1):

$$Swelling\ ratio = \frac{(W_s - W_D)}{W_s} \quad (1)$$

where W_S and W_D are the weights of the swollen and dried scaffolds, respectively.

2.3. Cytotoxicity assessment of adECM and adECM-rGO scaffolds

Lung A549, liver HepG2, and kidney HK2 cells were cultured in DMEM:F12 (Gibco, Paisley, UK), MEM containing sodium pyruvate (Gibco), or RPMI 1640 containing insulin-transferrin-sodium selenite and hydrocortisone (Gibco), respectively. Culture media were supplemented with 10% fetal bovine serum (FBS; Gibco), 1 mM L-glutamine (Lonza, Verviers, Belgium), 800 μg mL^{-1} penicillin (Lonza), and 800 μg mL^{-1} streptomycin (Lonza). To confirm cell morphology prior to cytotoxicity testing, cultures of each cell line were fixed and stained as previously reported [12]. In brief, samples were stained with Alexa Fluor 488-phalloidin (A12379; Thermo Fisher Scientific) and 3 μM 4′-6-diamidino-2′-phenylindole (DAPI) for 5 min to stain filamentous actin (F-actin) in green and cell nuclei in blue, respectively. Samples were examined using a FV1200 confocal laser scanning microscope (CLSM; Evident, Tokyo, Japan). Then, to determine potential cytotoxicity following direct contact with scaffolds, both adECM or adECM-rGO scaffolds were deposited on top of A549, HepG2, and HK2 confluent cell monolayers for 1 and 7 days in a 5% CO_2 humidified atmosphere at 37 °C, according to ISO 10993–5:2009. For each cell type, cell proliferation was quantified at both timepoints using the Cell Counting Kit-8 (CCK-8; Sigma), according to the manufacturer's instructions. Control conditions included a blank (media only), positive (culture media with cells), and a negative control (10% DMSO). For each condition, cell proliferation was measured using four replicates, of which each replicate consisted of six separate measurements.

2.4. Measurement of intracellular reactive oxygen species content and TNF-α secretion of RAW-264.7 macrophages

To determine intracellular reactive oxygen species (ROS), both adECM and adECM-rGO were deposited on top of RAW-264.7 macrophage confluent monolayers and cultured in DMEM, supplemented with 10% FBS, 1 mM L-glutamine, 800 μg mL^{-1} penicillin and 800 μg mL^{-1} streptomycin in a 5% CO_2 humidified atmosphere at 37 °C for 1 day. In parallel, control macrophages were cultured in the absence of scaffolds. Intracellular ROS was determined as previously reported [12]. Flow cytometric analysis was performed in three experiments, and each sample contained at least 10.000 cells. Additionally, secretion of tumor necrosis factor alpha (TNF-α) and interleukin 6 (IL-6) by RAW-264.7 macrophages cultured for 1 day in direct contact with both adECM and adECM-rGO scaffolds was determined by enzyme-linked immunosorbent assay (ELISA; bioNova científica, Madrid, Spain), according to the manufacturer's instructions. ELISA was performed in three separate experiments.

2.5. Assessment of macrophage polarization by flow cytometry and confocal microscopy

Potential polarization response of RAW-264.7 macrophages towards a pro-inflammatory M1 or reparative M2 phenotype was determined by flow cytometry and confocal microscopy. Flow cytometric analysis was performed as reported before [12], following the deposition of adECM and adECM-rGO on top of RAW-264.7 macrophage confluent monolayers for 1 and 2 days. Specifically, cells were incubated with Alexa Fluor 647-conjugated anti-mouse CD80 antibody (2.5 μg mL^{-1}; BioLegend, San Diego, CA, USA) and with Alexa Fluor 488-conjugated anti-mouse CD206 antibody (2.5 μg mL^{-1}; BioLegend) for 30 min, shielded from light. Labeled macrophages were then analyzed using a FACSCalibur flow cytometer (BD, Franklin Lakes, NJ, USA). Flow cytometric analysis was performed in three experiments, and each sample contained at least 10.000 cells. For confocal microscopy, macrophages cultured for 2 days on the surface of adECM and adECM-rGO scaffolds were fixed and stained with the above-mentioned antibodies. Samples were examined using a FV1200 CLSM.

2.6. Animals

Adult female Sprague-Dawley rats (n = 29) were provided by Envigo (cohort #1; n = 13; 208–240 g; Horst, The Netherlands) and Charles

River (cohort #2; n = 16; 250–307 g; 's-Hertogenbosch, The Netherlands). All procedures adhered to the regulations for animal experimentation in the Dutch Experiments on Animals Act (Wod) and the European Union (directive 2010/63/EU) and were approved by the Dutch Central Authority for Scientific Procedures on Animals (CCD; AVD10300202114868). Rats were housed in groups (of 2–3 animals) at a 12h light/dark cycle with food and water *ad libitum*.

2.7. Surgical procedures

Carprofen (3.33 mg kg^{-1}; Bela-Pharm, Vechta, Germany) was subcutaneously injected pre-operatively, and post-operatively for two days. All surgical procedures were performed under inhalation anaesthesia with isoflurane (3–5% induction; 1.5–2.5% maintenance in 1:2 O_2/air). Prior to skin incision (approx. 2–3 cm), bupivacaine (1.67 mg kg^{-1}; Aurobindo, Baarn, The Netherlands) and lidocaine (3.33 mg kg^{-1}; Fresenius Kabi, Bad Homburg, Germany) in 0.9% sterile NaCl were subcutaneously injected to provide local analgesia. Subcutaneous fat tissue and paraspinal muscles were then dissected to expose the T8-T11 region of the spinal column. Upon identification and subsequent removal of the T10 spinous process, a micro-rongeur (Fine Science Tools, Heidelberg, Germany) was used to generate the laminectomy (2.5 mm by 2 mm). Two independent surgeons performed the laminectomy procedures, blinded to treatment conditions. Rats were randomly divided over the following treatment groups: laminectomy-only (Control, n = 6), laminectomy and adECM implantation (adECM, n = 12), and laminectomy and adECM-rGO implantation (adECM-rGO, n = 11). Upon completion of the laminectomy, the treatment group of that specific animal was revealed, followed by scaffold implantation on top of the exposed spinal cord (in case of the 'adECM' and 'adECM-rGO' groups). In case of the control condition, no scaffold was implanted into the laminectomy site. Buprenorphine (0.015 mg kg^{-1}; richter pharma, Wels, Austria) was subcutaneously injected 15 min prior to waking up. Then, deep and superficial muscles were carefully approximated using 4-0 synthetic absorbable sutures (Ethicon, Raritan, NJ, USA), followed by closure of the skin (EZ Clips; Stoelting, Dublin, Ireland). During the first 7 post-operative days, and weekly thereafter, animals were weighed, and welfare was extensively checked using a self-established registration document, monitoring signs of pain and distress, dehydration, respiratory failure and mobility issues.

2.8. Blood sampling and analysis

Following 1 week of housing, blood (approx. 600 μL) was collected through tail vein sampling, stored in anticoagulant tubes (BD, Temse, Belgium) and centrifuged (1500g; 10 min; 4 °C). Plasma was subsequently stored at −80 °C until analysis. At the end of the experimental period (6 weeks), rats were sacrificed by cardiac puncture to draw blood (approx. 3–5 mL). Blood samples were collected in anticoagulant tubes (BD), centrifuged (1500g; 10 min; 4 °C), and plasma was stored at −80 °C until analysis. Plasma total protein (TP), cholesterol (CHOL), triglycerides (TG), glucose (Glc), albumin (ALB), alkaline phosphatase (ALP), alanine aminotransferase (ALAT), aspartate aminotransferase (ASAT), gamma-glutamyltransferase (GGT), creatine kinase-myocardial band (CK-MB), creatinine (CREAT) and urea (UREA) were quantified in a chemistry analyzer (Prestige 24i; Cormay, Warsaw, Poland).

2.9. Histological processing

Following 6 weeks of implantation, animals were sacrificed by cardiac puncture. Upon subsequent systemic perfusion with PBS, the lungs, liver, kidneys, spleen, and brain were excised. Organs were first weighed, then photographed for macroscopic analysis, and subsequently fixed in 10% neutral buffered formalin for 48h. Spinal columns corresponding to 5–7 vertebrae were excised, fixed in 10% neutral buffered formalin for 48h and subsequently decalcified in 10 % EDTA (Sigma) for two weeks. Organs and spinal columns were then dehydrated through graded series of ethanol, cleared with xylene and finally embedded in paraffin. Sections (5 μm thickness) were cut at three or five representative levels (at least 100 μm apart) for organs and spinal columns, respectively.

2.10. Histology

To assess the FBR as well as potential accumulation of degradation products and organ inflammation, tissue and organ sections were used for routine hematoxylin and eosin (H&E) staining. In addition, a Masson-Goldner's trichrome stain was performed to visualize fibrosis and potential fibrotic encapsulation of the scaffolds. Following both histological stainings, samples were dehydrated through graded series of ethanol, mounted and subsequently scanned using the PANNORAMIC 1000 slide digitalization system (3DHISTECH, Budapest, Hungary). Automatically scanned slides were evaluated in CaseViewer (3DHISTECH) by an independent pathologist, blinded to treatment condition. In brief, potential cell infiltration, inflammation, granuloma formation and fibrous encapsulation were evaluated for each implantation site. Organ sections were assessed for signs of inflammation, structural damage, and accumulation of degradation products.

2.11. Immunohistochemistry

Immunohistochemistry was performed to identify both M1-polarization marker CD86 and M2-polarization marker CD163, in a similar fashion as described earlier [32]. In brief, sections were heated in citrate buffer (10 mM; pH 5.85; Sigma-Aldrich) for 10 min, followed by 5 min of trypsin incubation (0.075%) at 37 °C. Samples were incubated with mouse anti-rat CD163 antibody (1:25; MCA342, Bio-Rad, Veenendaal, The Netherlands), followed by incubation with a secondary biotin-conjugated donkey anti-mouse antibody (1:500; 715-065-151, Jackson ImmunoResearch, Cambridge, UK). Upon peroxidase (PO) detection with H_2O_2 and 3,3′-diaminobenzidine (DAB, Sigma-Aldrich) for 10 min, sections were incubated with rabbit anti-rat CD86 (1:800; NBP2-67417, Bio-Techne, Abingdon, UK), overnight at 4 °C. Samples were then incubated with β-galactosidase (β-gal)-conjugated goat anti-rabbit antibody (1:100; ab136774; abcam, Cambridge, UK) for 1h at RT, and β-gal detection with 5-bromo-4--chloro-3-indolyl-β-D-galactoside (BCIG) was performed as previously reported [33]. Sections were incubated with this reaction mixture for 60 min at 37 °C. All samples were counterstained using nuclear fast red (Polysciences, Warrington, PA, USA), mounted and subsequently imaged using an AxioImager Z2 (Zeiss, Oberkochen, Germany). For each treatment condition, n = 6 animals were randomly selected for analysis. Cells staining positive for M2, while being present within a predefined region of interest (n ≥ 5 per animal), were quantified and average cell density was presented as number of cells per mm^2.

2.12. Statistical analysis

Compressive Young's modulus and PBS uptake characterization were evaluated by one-way analysis of variance (ANOVA). Regarding the assessment of cytotoxicity, intracellular ROS content and secretion of TNF-α and IL-6, results were presented as the means of three identical experiments. For these measurements, statistical analysis included ANOVA and Scheffé and Games-Howell post-hoc assessment to compare experimental groups. For quantification of macrophage density *in vivo*, analysis included ANOVA and Bonferroni post-hoc comparison. For all statistical assessments, a p-value <0.05 was considered as statistically significant.

3. Results and discussion

3.1. Scaffold synthesis and characterization

Partial reduction of GO was performed by thermal annealing. As shown by XPS analysis (Fig. 1A), thermal reduction mostly affected inherently unstable in-plane oxygen containing groups, notably removing the hydroxyl and epoxy groups as per the evident decrease of the XPS peaks area related to both C–O (286.7 eV) and O–C═O (288.7 eV) oxygenated components [34], while producing new C–H and C═C bonds (284.6 eV). Also, owing to the partial restoration of the sp^2 graphitic structure, the contribution of π–π transition (290.1 eV) increased. More details on the characterization of rGO can be found elsewhere [20]. This thermal annealing yielded rGO nanosheets, still offering enough remanent oxygen moieties to provide abundant reactive sites for rGO to interact with the adECM proteins through hydrogen bonding, π–π and hydrophobic interactions, wherein the aromatic benzene ring structure served for orienting hydrophobic residues of the matrix components towards the rGO sheets surface. Partial reduction was not only critical to provide structural integrity for the scaffolds with

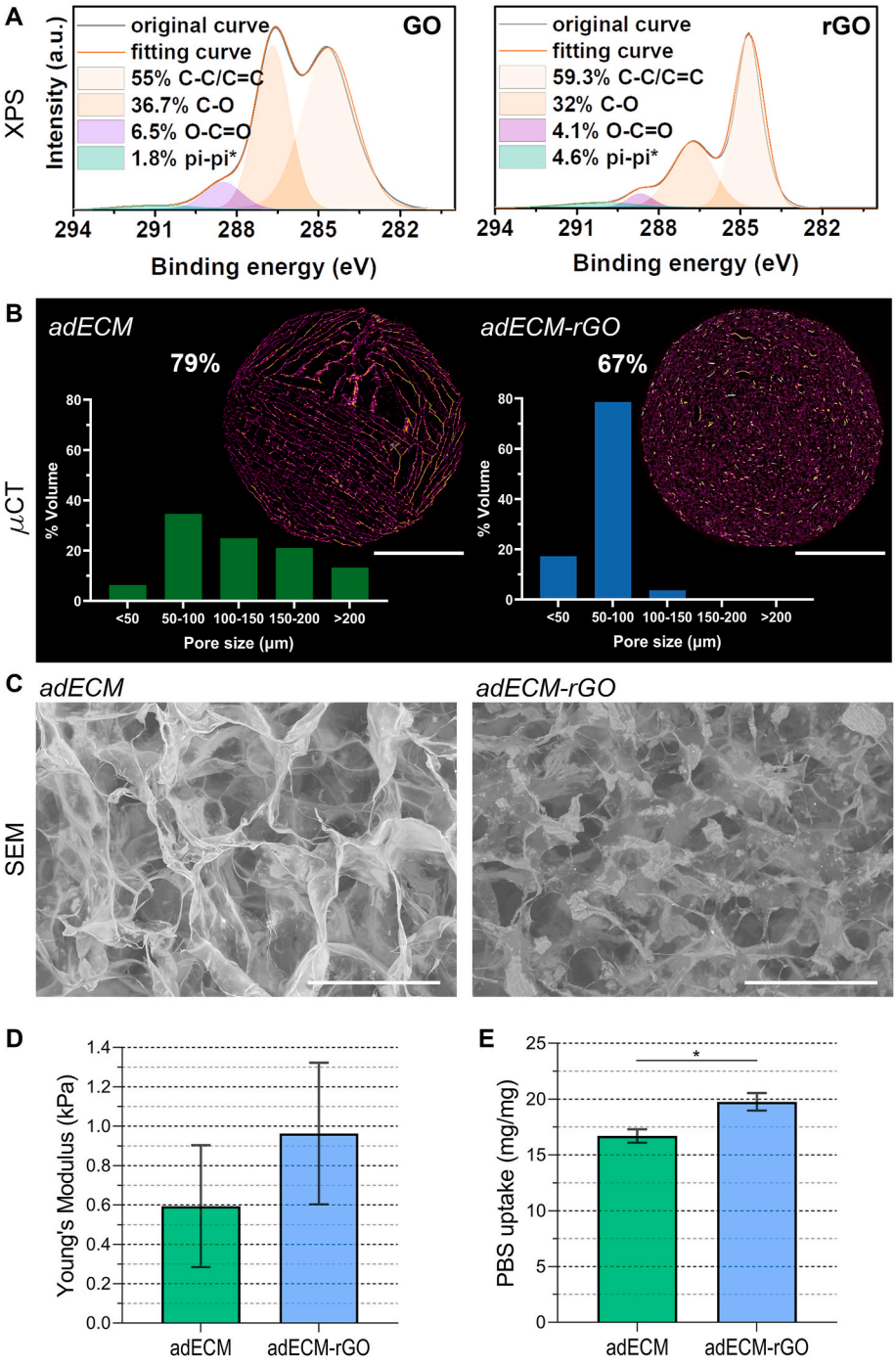

Fig. 1. Synthesis and characterization of adECM and adECM-rGO scaffolds. A) Characterization of GO (left) and rGO (right) via X-ray photoelectron spectroscopy; B) Morphological characterization of the adECM and adECM-rGO solid foams, including reconstructed foams top view from μCT projections (scale bar: 2 mm) with representative graphs of the percentage pore volume depending on pore ranges based on μCT morphometric data; C) scanning electron microscopy of the foams cross section (scale bar: 200 μm); D) Compressive Young's modulus; E) PBS uptake at equilibrium.

high contents of rGO (50 wt%), but also improved the biocompatibility compared to complete reduction or non-reduced forms of GO [35]. Processing adECM did not result in protein denaturation, as confirmed by CD spectroscopy (Fig. S1). Here, both the negative peak, corresponding to the random coil, and a positive peak at 222 nm, corresponding to the triple helical structure of native collagen, showed the intact tertiary structure of proteins when processing adECM.

Solid-liquid phase separation by ice templating/freeze casting is a simple and effective process that can be used to fabricate scaffolds of particular porosity and pore size, in order to facilitate optimal cellular infiltration, growth and nutrient flow [36,37]. In a previous study, we prepared porous constructs of rGO-modified adECM with up to 50 wt% of rGO, which were shown to induce neuronal differentiation of neural progenitor cells in an rGO dose-dependent manner [20]. Given this promising *in vitro* response in the context of neural regeneration, adECM scaffolds and adECM-rGO composites with 50 wt% of rGO were selected for further safety studies. However, these adECM and adECM-rGO scaffolds previously presented significant structural differences, such as macroscopic mechanical properties and water uptake capacity. For instance, adECM scaffolds exhibited a Young's modulus nearly 3-fold higher than their counterparts with 50% of rGO [20]. In view of focusing on the specific role of rGO upon implantation, and since scaffold porosity and stiffness are functional determinants of tissue response, it is preferable to implant constructs with similar structural and mechanical characteristics [37,38]. Therefore, in this study, relevant factors of the ice templating process – solvent molarity of the polymer/solvent system and mold size – were purposedly regulated to guide the mechanisms of the thermodynamic-driven phase separation, in order to narrow down these structural differences.

The crystallite geometry serves as the porosity template for the scaffold following freeze-drying. In the present study, two different slurry systems were used, i.e. the adECM/acetic acid system and the adECM/rGO/acetic acid system. The latter differed in terms of adECM amount and rGO incorporation, which yielded a slurry with a lower viscosity. Morphological analysis encompassed μCT morphometric analysis and SEM analysis (Fig. 1B and C). In the adECM scaffolds, mechanisms of phase growth were visibly more active as confirmed by a broader pore size distribution with more than 30% of pores larger than 150 μm. Since the adECM/acetic acid system had a higher adECM concentration in comparison to the adECM/rGO/acetic acid system, more macromolecules of adECM were available and concentrated around the growing solvent crystallites. This subsequently affected the shape of the solvent crystallites, which together with large differences in the slurry cooling rate within the system [39] contributed to create anisotropic porosity with radially aligned pores (Fig. 1B). Indeed, it has previously been demonstrated that for systems with high concentrations of proteins, macromolecules concentrating around the growing solvent crystallites yield well-defined lamellar pores [40]. In the current study, for the adECM-rGO composites, the applied multidirectional freezing yielded the commonly observed isotopically oriented crystals without a specific predominant pore orientation [40]. Specifically, this resulted in a smaller global porosity (67%) than adECM scaffolds (79%), along with narrower pore size distribution (around 95% of pores below 100 μm), which is characteristic of systems with lower polymer concentrations. Both types of scaffolds presented a homogenous pore distribution, as confirmed by SEM analysis (Fig. 1C).

Importantly, the distinct pore structure found in the present study mitigated the differences in mechanical properties of both types of scaffolds observed before [20]. The hierarchical structure of lamellar pores, observed in adECM scaffolds, was previously shown to significantly reduce Young's modulus when oriented in a curved manner or perpendicularly to a compressive loading force [41]. Accordingly, in the current study, both scaffolds presented a similar Young's modulus, i.e. 0.59 ± 0.31 kPa and 0.97 ± 0.36 kPa for the adECM and adECM-rGO composites, respectively (Fig. 1D). Furthermore, oscillatory shear rheology revealed that adECM scaffolds exhibited a storage (0.62 ± 0.09 kPa) and loss modulus (0.07 ± 0.01 kPa) within a similar range, as compared to the storage (0.61 ± 0.10 kPa) and loss modulus (0.05 ± 0.01 kPa) of adECM-rGO scaffolds (Fig. S2). It is considered critical that these scaffolds are mechanically compliant with the healthy rat spinal cord, as distinct mechanical properties can increase astrogliosis and affect neuronal regrowth [38]. Recently, mechanically compliant rGO aerogels, prepared also by ice-templating/freeze-drying, were implanted following the hemisection of a rat cervical spinal cord [19]. After 4 months, these aerogels were completely vascularized and populated with neurites, some of them being myelinated excitatory axons. Finally, also water uptake (Fig. 1E) was characterized, as an important criterion to indirectly predict how easily cells will infiltrate the scaffolds. Despite the lower overall porosity along a narrower distribution of smaller pores, adECM-rGO composites had a slightly higher PBS uptake. This was expected since water molecules partially disrupt intermolecular forces between rGO and the adECM subsequently inducing a larger swelling. All in all, by varying solvent molarity and mold size, scaffolds with similar structural and mechanical properties were constructed.

3.2. Cytotoxicity and immune response in vitro

To determine the biological response of mammalian cells to the scaffolds, potential pulmonary, renal and hepatocytotoxicity of adECM and adECM-rGO scaffolds were evaluated *in vitro* in line with ISO standard 10993-5-2009. Epithelial-like morphology of all three cell lines was first confirmed (Fig. 2A). With respect to the control condition, cell proliferation (Fig. 2B) remained unaffected following culture in direct contact with either adECM or adECM-rGO scaffolds. Regarding HepG2 and HK2 cell lines, gradual depletion of nutrients could have resulted in the reduced proliferation seen after 7 days. After cells were directly exposed to the scaffolds, the cultures were examined by confocal microscopy and no morphological alterations were observed, with the epithelial-like cell appearance of each cell type similar to the images presented in Fig. 2A. Anticipating adECM and adECM-rGO implantation and subsequent protein adsorption [22], macrophages are the primary responding cell type and, depending on their phenotypic state, exhibit critical regulatory activity during all stages of tissue repair and fibrosis [42]. Whereas classically activated M1 macrophages are typically involved in the intracellular killing of pathogens and secretion of pro-inflammatory cytokines, alternatively activated M2 macrophages produce anti-inflammatory factors and are involved in tissue remodeling during wound healing [42]. Here, intracellular ROS content (Fig. 2C), indicative of oxidative stress [28], and secreted TNF-α (Fig. 2D), a pro-inflammatory cytokine [43], remained unaltered with respect to the control. However, direct culture with adECM-rGO led to a substantial increase in levels of IL-6 (Fig. 2E) secreted by macrophages, which was not observed for adECM scaffolds. Generally regarded as a pro-inflammatory (M1-like) factor, IL-6 is a pleiotropic cytokine with both beneficial and destructive roles [44]. Nevertheless, macrophages that were cultured on top of both types of scaffolds did not demonstrate distinct expression of CD80 (M1; Fig. 2F) or CD206 (M2; Fig. 2G), as determined by fluorescence microscopy. Flow cytometric analysis did show significantly decreased expression of CD80, for both scaffolds (Fig. 2H), and CD206, for adECM-rGO only (Fig. 2I), which recovered following 48h of culture. Therefore, it can be concluded that both adECM and adECM-rGO scaffolds did not induce a pro-inflammatory response *in vitro*. In line with the present work, cells involved in the innate and adaptive immune system were previously exposed to rGO nanoparticles. The cytocompatibility of these rGO sheets was superior when cultured in contact with macrophages [28] and did not alter the response of Th2 lymphocytes [45]. In conclusion, our cytocompatibility assays warranted further preclinical evaluation of the biocompatibility of both scaffolds following *in vivo* implantation.

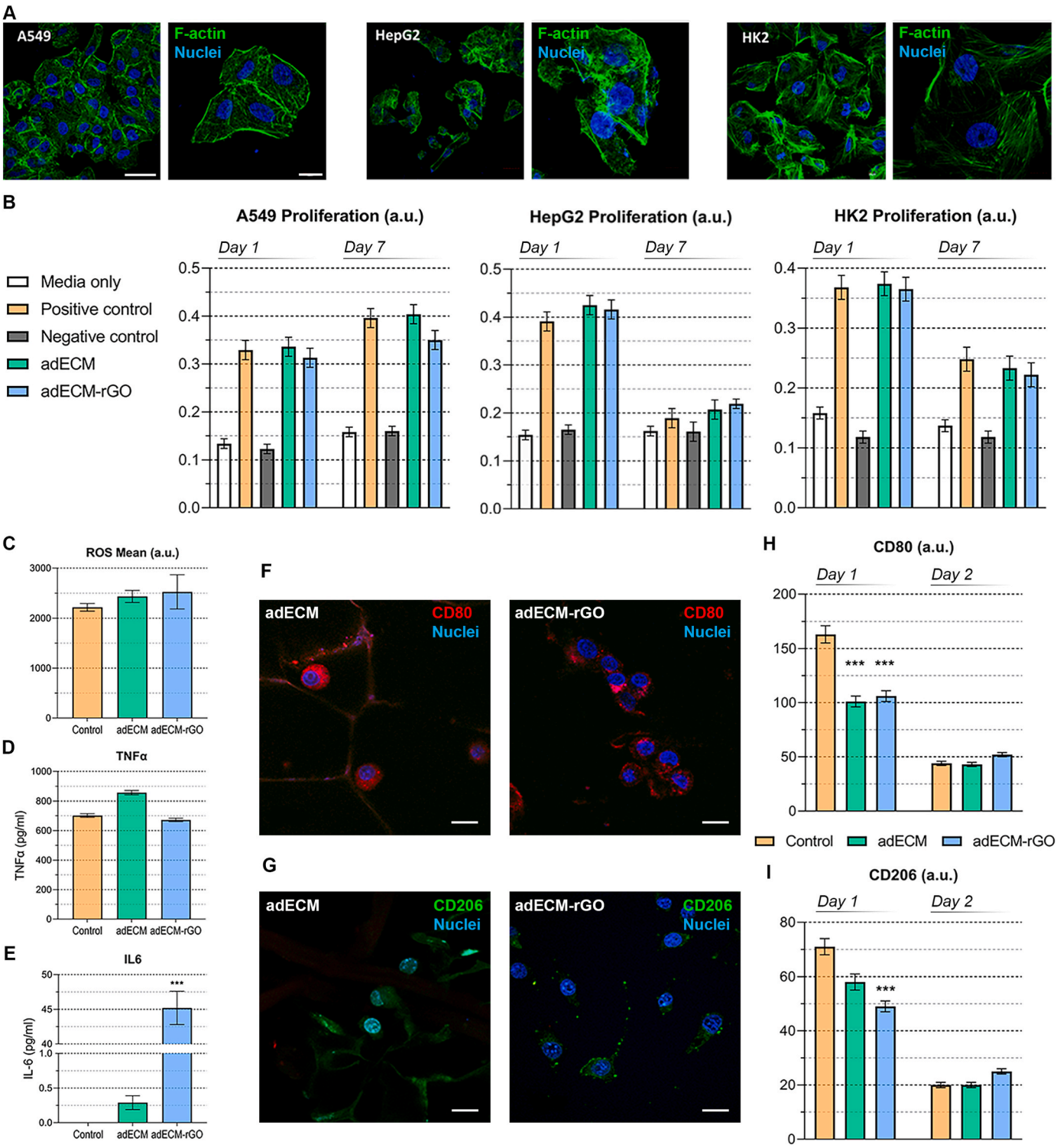

Fig. 2. Cytotoxicity and immune response following direct contact with adECM and adECM-rGO scaffolds. A) Confocal microscopy images confirming cell morphology of lung A549, liver HepG2, and kidney HK2 cells from left to right, respectively. Nuclei are labeled in blue, while filamentous actin (F-actin) is stained green. Scalebar represents either 20 μm (left), or 5 μm (right), which applies to all cell lines. B) CCK-8 assay results following 1 and 7 days of culture in direct contact with adECM and adECM-rGO scaffolds for lung A549, liver HepG2, and kidney HK2 cells, from left to right, respectively. Positive control corresponds to culture media and cells, while the negative control corresponds to 10% DMSO. Following direct contact culture of RAW-264.7 macrophages with adECM and adECM-rGO scaffolds, intracellular content of ROS, measured by flow cytometry, and secretion of TNFα and IL-6, measured by ELISA, is presented in (C), (D), and (E), respectively. Confocal microscopy images depict the morphology of RAW-264.7 macrophages (F, G), cultured on the surface of adECM (left) and adECM-rGO (right) scaffolds. Nuclei are labeled in blue, CD80 (F) is labeled in red and CD206 (G) is labeled in green. Scalebar represents 20 μm. Flow cytometry results are presented of CD80 (H) and CD206 (I) expression by RAW-264.7 macrophages, cultured for 24h and 48h on adECM and adECM-rGO scaffolds. (For interpretation of the references to color in this figure legend, the reader is referred to the Web version of this article.)

3.3. Integration and cellular infiltration in vivo

For *in vivo* experiments, a laminectomy at the 10th thoracic vertebra was performed in 3-month old female Sprague-Dawley rats. This study design was justified by: 1) our recent systematic review which showed that this model precedes one of the most used and most reliable animals models of SCI [46], and 2) previous observations that confirmed rats demonstrate spontaneous locomotor recovery until 3 months of age [47]. Laminectomy and subsequent scaffold implantation were successfully performed (Fig. 3A). Out of a total of 29 rats, only one animal was excluded one day after surgery due to an intestinal/stomach hemorrhage caused by the ingestion of bedding material. Administration of buprenorphine is known to potentially cause such pica behaviour in rodents [48], hence its dosage (0.03 mg/kg) was subsequently halved (0.015 mg/kg). Over the course of the experiment, all rats gradually gained weight (Fig. S3A). The majority of signals indicative of pain or distress as well as any functional deficits remained absent throughout the experimental period. Abnormalities in animal fur or the surgical wound, as well as a developed edema, all quickly resolved during the initial experimental stages (Fig. S3B). Despite the fact that conventional laminectomy produces trauma leading to various post-operative complications [49], these results showed that neither the laminectomy procedures nor implantation of either adECM or adECM-rGO scaffolds exerted a negative effect on animal welfare.

Generally, implantation of biomaterials unavoidably induces a FBR which typically includes immune cell infiltration and fibrous encapsulation. Therefore, biomaterial-based therapeutics should accommodate an acceptable degree of FBR without inducing severe FBR which leads to tissue degeneration [50]. Scaffold integration was first evaluated in axial sections of spinal columns (Fig. 3), which revealed a detailed overview of the implantation area. The shape of the spinal cord for the different groups appeared uniform and was not subject to physical stress through swelling of the surrounding tissues (Fig. 3B) and/or the implanted material (Fig. 3C and D). After 6 weeks of implantation, the adECM material was largely degraded or remodeled and replaced by other types of tissue (Fig. 3C), demonstrating the excellent biodegradability of naturally derived materials [2,9]. However, to achieve successful regeneration, scaffold degradation must match the rate of new tissue formation. Reinforcing scaffolds with GO has previously been suggested to slow down degradation rates [51]. In line with these observations, in the current study, the adECM-rGO scaffolds did not entirely degrade, since the rGO fraction was still observed after 6 weeks

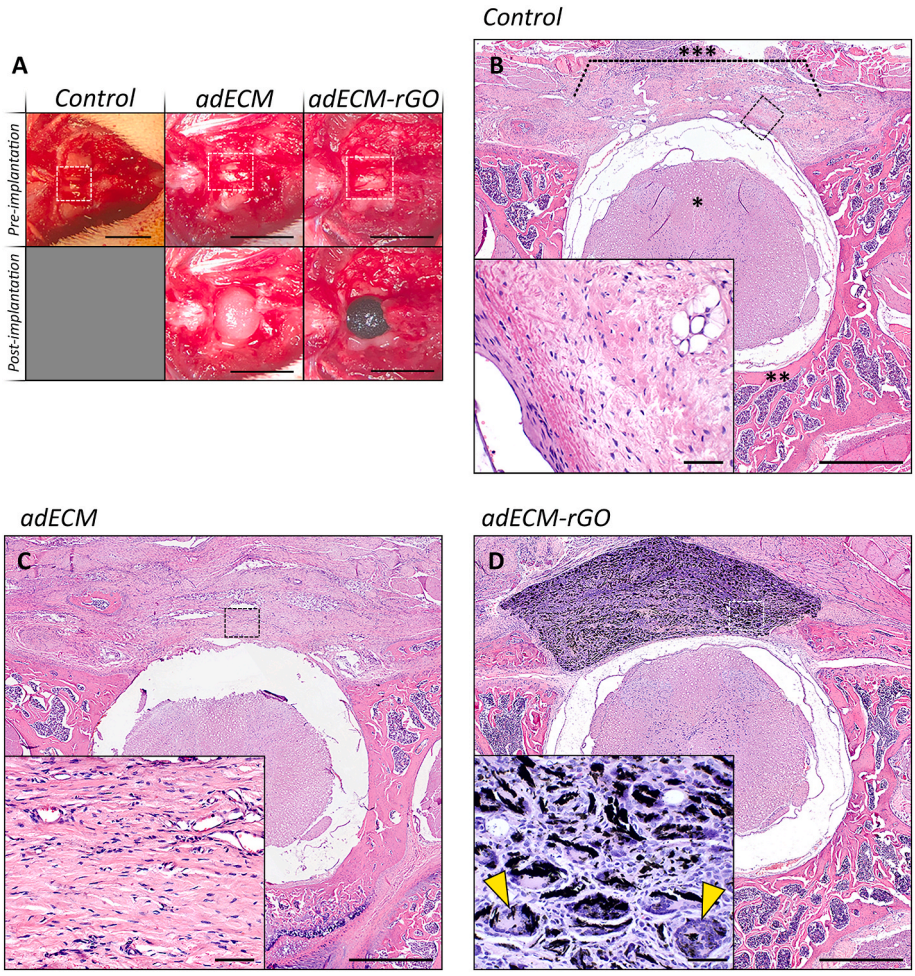

Fig. 3. Macroscopic and histological evaluation of the implantation site. Panel A shows pictures that were taken during surgery, before and after implantation for the control (left), adECM (middle), and adECM-rGO (right) treatment groups. Note that for each group, dotted line squares represent the site of laminectomy, in which the exposed spinal cord can be observed. Scalebar represents 0.5 cm. Axial tissue sections, stained with H&E, are presented for the control (B), adECM implantation (C), and adECM-rGO implantation groups (D). These transversal overview images depict the spinal cord (indicated by *), which is surrounded by the vertebra (**). Dorsal to the spinal cord, the site of laminectomy and implantation (***) can be distinguished. Inserts are included to present a more detailed view of cells infiltrating the injury site, represented by dotted line squares. Regarding the adECM-rGO group, yellow arrows show foreign body giant cells (FBGCs) that engulf rGO sheets. Scalebar represents either 1000 μm or 50 μm (inserts). (For interpretation of the references to color in this figure legend, the reader is referred to the Web version of this article.)

of implantation (Fig. 3D). The entire substrate area of adECM-rGO scaffolds was strongly cellularized, suggesting the pore size was appropriate for cell penetration [37]. In contrast, GO/collagen hybrids (130 μm in pore size) demonstrated lower levels of cell infiltration 8 weeks after implantation [51]. The more aggregated nature of rGO used here could have enhanced immune cell penetration [29]. Nevertheless, the fact that the implants demonstrated such abundant cell infiltration contradicts the potential toxicity of the materials used.

Macrophages that infiltrated the adECM-rGO composite fused to form multinucleated foreign body giant cells (FBGCs) to engulf larger-sized rGO nanosheets (Fig. 3D). This process is known to be a late-stage hallmark of the FBR [22] and has been often observed in pre-clinical applications of GBMs [51,52]. FBGCs are known to contribute towards material degradation through intracellular phagocytosis [53] and extracellular degradation [54], depending on the size of the particle [23]. Moreover, GBMs in general can undergo both hydrolytic and enzymatic degradation [13]. For instance, neutrophils are capable of degrading GO *in vitro* through a myeloperoxidase-dependent mechanism within hours [55]. In the present study, FBGCs contained either larger-sized, seemingly intact, rGO agglomerates, as well as smaller-sized sheets of rGO (Fig. S4). However, assuming rGO sheets were of similar size at the time of scaffold implantation, it is speculated that FBGCs contributed towards the breakdown and clearance of rGO sheets. To fully elucidate on the biodistribution and biodegradation of rGO, the material should be labeled and scaffolds should be evaluated at both early (days to weeks) and later experimental timepoints (months to a year), but this was beyond the scope of the current study. Although formation of FBGCs is often associated with aseptic loosening and material failure [56], degradation and subsequent elimination of the material can also be regarded desirable with the purpose of regenerating and replacing lost tissue. Hence, both types of scaffolds demonstrated substantial cellular infiltration, but formation of FBGCs and its effect on potential regeneration requires further investigation.

3.4. Immune response following adECM and adECM-rGO implantation

Understanding the phenotypic switch of macrophages infiltrating implanted scaffolds is crucial in the successful development of tissue-engineered constructs [57]. In regards of biomaterial-mediated tissue regeneration, polarization of infiltrating macrophages towards a regenerative M2-phenotype would be beneficial [58]. Following laminectomy (Fig. 4A) and adECM implantation (Fig. 4B), immunohistochemical assessment revealed a predominant polarization towards the M2-phenotype, indicating these cells participated in tissue remodeling to establish a pro-regenerative environment [42]. Similarly, M2-polarized macrophages were distributed throughout adECM-rGO scaffolds (Fig. 4C). Designing scaffolds of specific pore sizes previously stimulated macrophages to adopt the M2-phenotype [59], and adECM-rGO composites fell within this range at the time of implantation. The slowed down degradation rate of adECM-rGO suggested here could have caused pore sizes to remain intact for extended periods of time, thereby promoting M2-polarization (Fig. 4D). Still, prolonged presence of M2 macrophages could potentially stimulate formation of FBGCs [22,60], hence polarization should be tightly regulated. It is important to note that CD86 expression, albeit to a low extent, was observed in a fraction of FBGCs inhabiting the nanocomposites. CD86 is a lymphocyte co-stimulatory molecule and could therefore be associated with chronic inflammation [61]. This observation emphasizes the

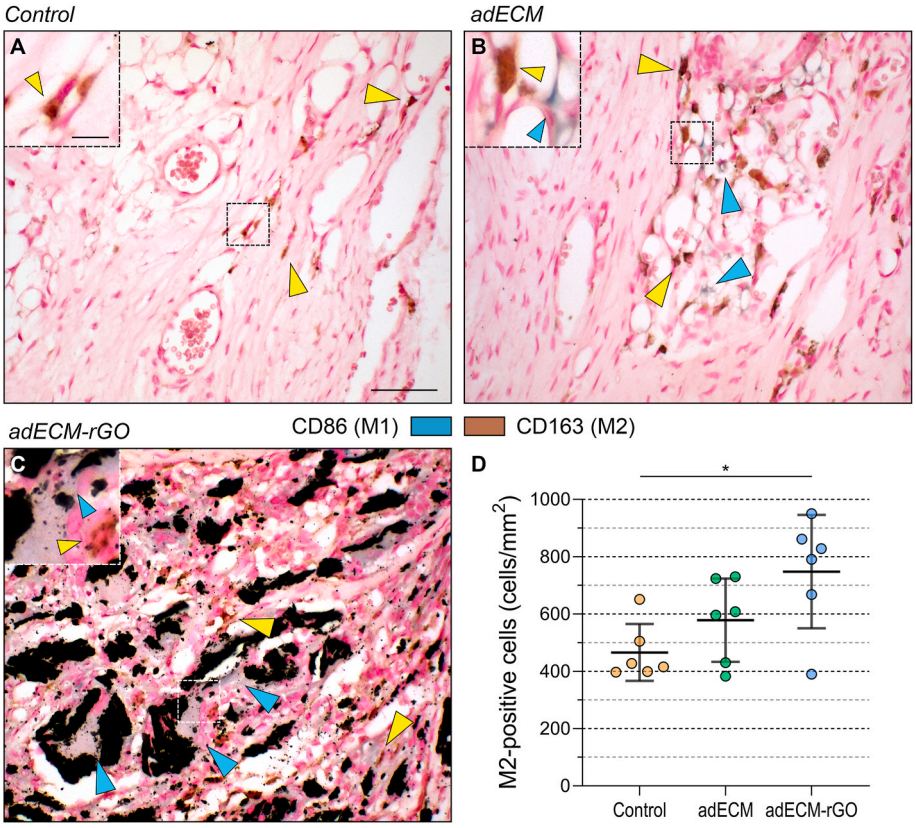

Fig. 4. Immunohistochemical assessment of macrophage polarization. Shown are immunohistochemical stainings of the implantation sites of the control (A), adECM (B) and adECM-rGO (C) treatment groups. For each treatment condition, cells positive for M1-marker CD86 are stained blue, while cells positive for M2-marker CD163 are stained brown. Higher magnification images (inserts) are represented by dotted line squares. For clarification, blue and yellow arrows represent M1-and M2-positive macrophages, respectively. Regarding adECM-rGO, it is noteworthy that foreign body giant cells (FBGCs) seem to express CD86. Scalebar represents either 50 μm or 10 μm (inserts). Quantification of M2-positive macrophage density in cells permm^2 (n = 6 for each treatment group) is presented in panel D. (For interpretation of the references to color in this figure legend, the reader is referred to the Web version of this article.)

importance of future research to investigate to what extent the regenerative potential of these nanocomposites is affected by the distribution of macrophage phenotypes presented herein [57]. Regarding tissue regeneration, scaffolds should ideally be vascularized, allowing for the diffusion of molecules to a greater extent [62]. Extensive neo-vascularization was observed in all treatment groups, including adECM and adECM-rGO (Fig. S5), which was previously reported for GBMs [19,52]. The fact that vasculature was observed in close proximity to FBGC-encapsulated rGO sheets suggests a tissue-regenerative environment.

3.5. Fibrotic response to adECM and adECM-rGO scaffolds

In addition to angiogenesis, deposition of ECM is a key characteristic of the desired reparative environment. Here, provisional matrix is converted into mature collagen-III rich ECM, which is eventually remodeled into collagen type I-rich fibrous tissue [63]. Presence of collagenous ECM, as evidenced by Masson-Goldner staining (Fig. 5), was observed in all treatment groups. Control groups generally demonstrated the deposition of connective tissue (Fig. 5A) and fibrotic scarring within the site of the laminectomy (Fig. 5B). Although the adECM implants could not be distinguished following 6 weeks of implantation (Fig. 5C), inflammation and fibrosis (thickness of 63.3 ± 11.4 μm) were observed to be more frequently present (Fig. 5D and G), compared to the adECM-rGO treatment group. Concerning adECM-rGO composites, matrix production was observed throughout the implant (Fig. 5E), often in a certain orientation (Fig. S6A and S6B), and was not observed to be of a fibrotic, acellular character. This orientation was observed to be more prominent in

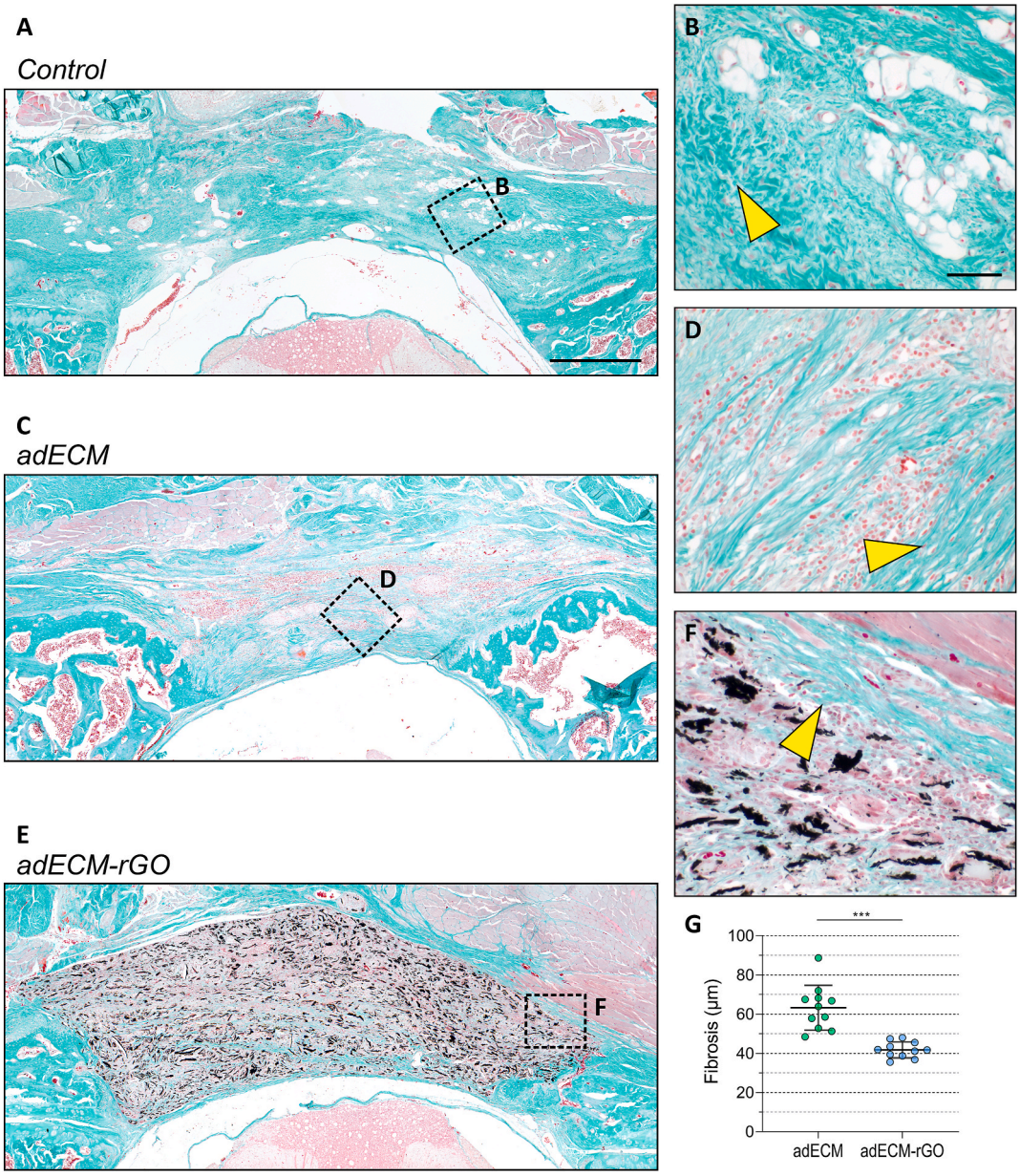

Fig. 5. Goldner-modified Masson's Trichrome staining of implantation area. To visualize fibrosis and fibrous encapsulation, a Masson-Goldner staining was performed for all treatment groups, including the control (A, with higher magnification image in B), adECM (C, with higher magnification image in D), and adECM-rGO (E, with higher magnification image in F). Higher magnification images are represented by dotted line squares. Collagenous fibrous tissue is stained green, nuclei are stained red. Concerning the higher magnification images, yellow arrows specifically depict fibrosis (D) or fibrotic encapsulation (F). Scalebar represents 500 μm (A-C-E) or 50 μm (B-D-F). Panel G shows the quantification results of fibrosis (in μm) regarding the adECM and adECM-rGO treatment groups. (For interpretation of the references to color in this figure legend, the reader is referred to the Web version of this article.)

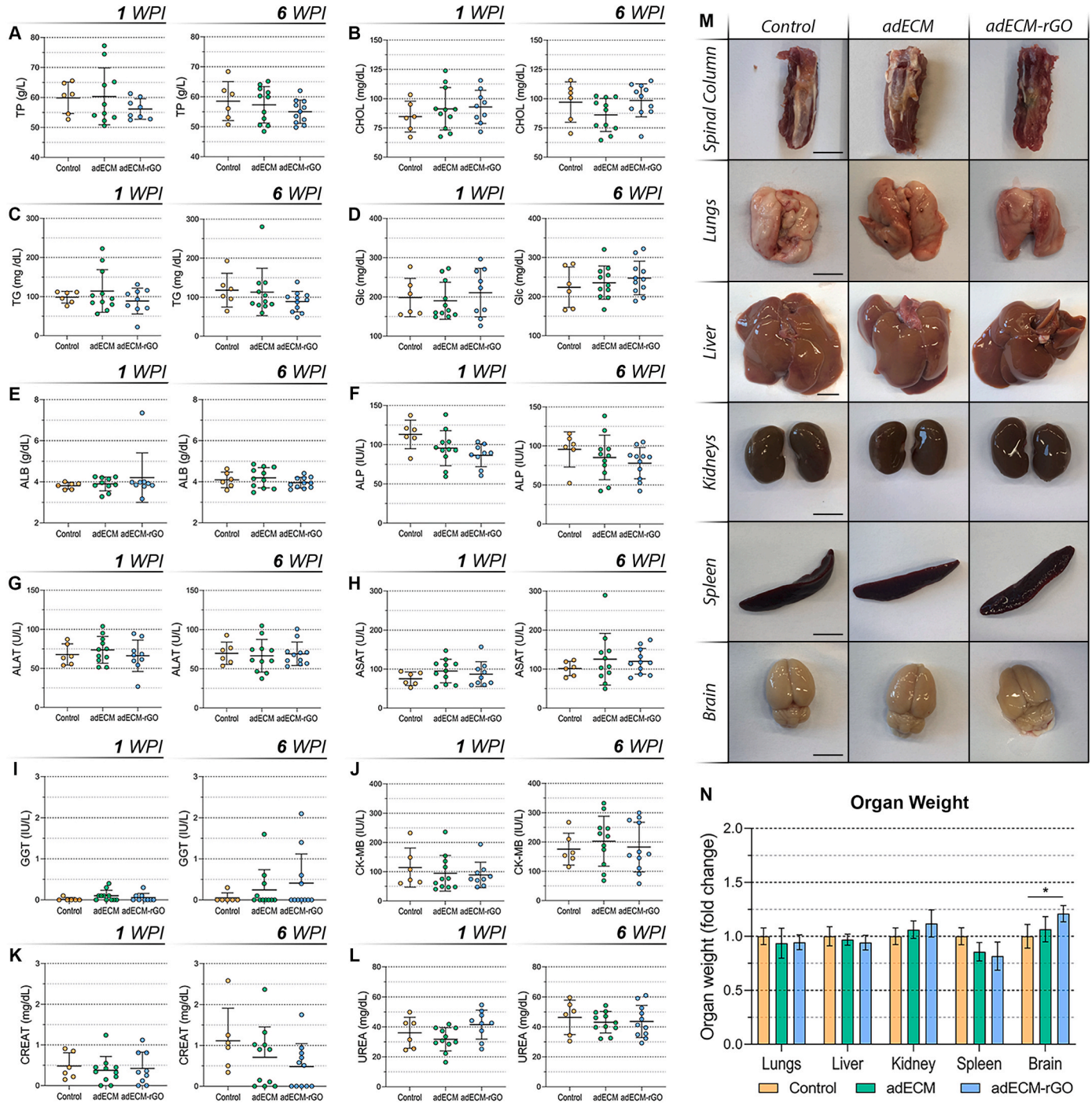

Fig. 6. Biochemical plasma analysis and macroscopic assessment of relevant organs. For each timepoint, 1 (left) and 6 weeks (right) after implantation, plasma levels of total protein (TP; A), cholesterol (CHOL; B), triglycerides (TG; C), glucose (Glc; D), albumin (ALB; E), alkaline phosphatase (ALP; F), alanine aminotransferase (ALAT; G), aspartate aminotransferase (ASAT; H), gamma-glutamyltransferase (GGT; I), creatine kinase-myocardial band (CK-MB; J), creatinine (CREAT; K) and urea (UREA; L) are presented for the control, adECM and adECM-rGO groups. The spinal column, lungs, liver, kidneys, spleen and brain were harvested and pictures are presented in panel M (scalebar represents 1 cm). Organs weights at time of sacrifice are presented in panel N.

Table 1

Histopathological screening of relevant organs. Lung, liver, kidney, spleen, and brain tissue of the control (n = 6), adECM (n = 11), and adECM-rGO (n = 11) treatment groups was histopathologically screened by an independent pathologist. During screening, tissue sections of the control group were used as a reference for the adECM and adECM-rGO treatment groups. For each organ, n = 3 separate tissue sections (at least 100 μm apart) were screened. Note that lung tissue presented lymphoid cell infiltration, independent of treatment group, most probably caused by the use of inhalation anaesthesia during sacrifice.

Experimental Group	Lung	Liver	Kidney	Spleen	Brain
Control	Lymphocytic infiltration	No deviations	No deviations	No deviations	No deviations
adECM	Lymphocytic infiltration	No deviations	No deviations	No deviations	No deviations
adECM-rGO	Lymphocytic infiltration	No deviations	No deviations	No deviations	No deviations

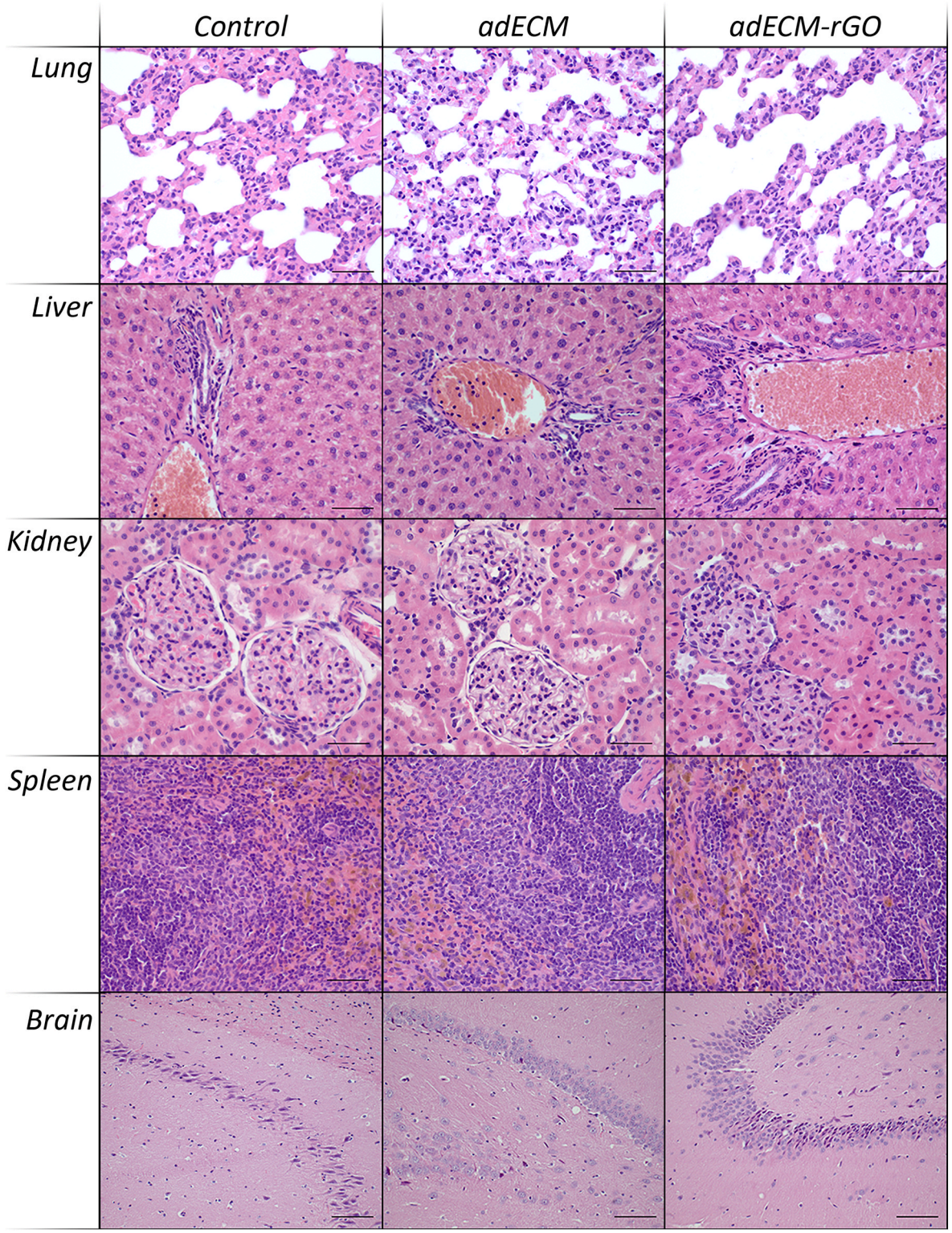

Fig. 7. Histological staining (H&E) of relevant organs. To check for potential organ inflammation, structural damage, or accumulation of material components, relevant organs from the control (left), adECM (middle) and adECM-rGO (right) treatment groups. Presented are H&E stainings of lung, liver, kidney, spleen, and brain tissue (from top to bottom). Scalebar represents 50 μm.

ventral regions of the scaffold (Fig. S6C and S6D), as compared to dorsally located sites (Fig. S6E and S6F), which was observed for adECM implants as well (Fig. 5C). The fact that remaining rGO sheets conform to this orientation indicated the ability of the host tissue to remodel the implanted scaffold according to the dimensions of the lesion site, as opposed to diffuse remodeling observed before [29,51]. This is of great importance envisaging the application in regenerating linearly oriented tissues, such as the spinal cord. In contrast, inflammatory cells seem to be more prominently present in dorsal regions of the implantation sites (Fig. 5C and Fig. S6A). Even though signs of chronic inflammation were abundantly present after 6 weeks of implantation, we speculate that the remodeling process is continuously ongoing in a gradual pattern from

ventral to dorsal implant regions.

Biomaterial integration can be hampered by severe encapsulation along with separation of the implant from the host tissue, greatly limiting any therapeutic potential [63]. Fibrotic encapsulation of adECM-rGO scaffolds (Fig. 5F) was more limited (thickness of 41.8 ± 4.07 μm) compared to its adECM counterpart (Fig. 5G). This can be explained from the fact that adECM scaffolds consisted of twice the amount of xenogeneic, porcine matrix, which could have evoked a stronger immunogenic response [2]. In addition, the increase in cross-linking agents used for adECM scaffolds could have contributed towards the elevated fibrotic response [64]. Accordingly, minor fibrotic encapsulation was previously observed following transcutaneous injection of rGO [29] or implantation of graphene-silk composites [52]. However, application of these materials still caused separation of the implants from the host tissue, which was not observed in the present research for both the adECM and adECM-rGO scaffolds. As summarized in Fig. S7, both types of scaffolds were well integrated into the host tissue and elicited only a very moderate FBR. To translate these encouraging safety results towards therapeutic applications, future research efforts should evaluate the efficacy of these scaffolds by including spinal cord associated markers.

3.6. Systemic compatibility and biodistribution

As a final point of concern, leachables or degradation products of rGO could potentially enter the circulation, accumulate at organ-specific sites, and initiate secondary organ damage or inflammation [65]. Nevertheless, blood plasma analysis revealed that whole-body metabolism (Fig. 6A–D) remained unaltered throughout the experimental period. Levels of circulating ALB (Fig. 6E) fell within standard reference values [66] and were unaffected by treatment condition, indicating the absence of inflammation. Furthermore, plasma analysis indicated that implantation of adECM nor adECM-rGO scaffolds attenuated liver, kidney, or heart function (Fig. 6F-L).

Macroscopic analysis of the implantation site (Fig. 6M) as well as relevant organs including lungs, liver, kidneys, spleen and brain, did not reveal any obvious abnormalities or distinct organ weights (Fig. 6N) between the adECM and adECM-rGO treatment groups. Whole-organ histopathological screening, as opposed to conventional microscopic analysis of only few representative organ sections, was performed to reliably rule out any secondary damage or inflammation caused by accumulation of rGO nanosheets (Table 1). In agreement with plasma assessment and previous reports involving application of rGO-based materials, no morphological deformities, such as inflammation, fibrosis or atrophy, were observed in the lungs, liver, kidneys, spleen, and brain tissue (Fig. 7) [19,67]. This absence of toxicity can be explained by several underlying factors. For instance, the implantation dose of rGO used here (150 μg per rat, corresponding to 0.53–0.67 mg/kg) was substantially lower compared to various previous reports (10–14.4 mg/kg) that showed organ-specific toxicity [31,68]. Nevertheless, in view of local implantation, the amount used here can still be regarded as substantial. However, this type of administration subjects rGO to biological functionalization by the host, inferring a completely different biocompatibility [29] and biodistribution profile [69]. Next to that, although FBGC-mediated clearance is speculated in the present study, the majority of rGO remained in the implantation site throughout the experimental period and could therefore not have entered the circulation. Yet, rGO will not remain permanently confined at the implant site. One of the very scarcely available studies addressing longer-term application of rGO-based scaffolds demonstrated the onset of sheet degradation at 1 and 4 months after implantation [19]. However, even with degradation being demonstrated, organ-specific accumulation and toxicity remained absent, in line with the lack of toxicity observed following *in vitro* biodegradation of GO [55]. Accordingly, throughout 6 weeks of adECM-rGO implantation, these nanocomposites demonstrated biocompatible responses within the systemic circulation.

4. Conclusions

Repairing the injured spinal cord requires the use of multifunctional biomaterials that are capable of treating various facets of this complex pathophysiology. To this end, the present research thoroughly investigated the safety and biocompatibility of both pristine adECM and rGO-modified adECM nanocomposites, which were previously shown to hold strong potential for treatment of SCI. We showed that both adECM and adECM-rGO scaffolds were cytocompatible *in vitro*, underscoring their suitability for further preclinical evaluation. Upon *in vivo* implantation, adECM scaffolds were either degraded or strongly integrated with host tissue. Notably, adECM-rGO nanocomposites exhibited limited fibrous encapsulation. Although rGO nanosheets were engulfed by multinucleated giant cells, histopathological screening did not detect any organ-specific accumulation or inflammation. Hence, both implants elicited a biocompatible response after 6 weeks of implantation and can therefore be considered for further translational studies on the treatment of SCI.

CRediT authorship contribution statement

Kest Verstappen: Writing – review & editing, Writing – original draft, Visualization, Methodology, Investigation, Formal analysis, Data curation. **Alexey Klymov:** Writing – review & editing, Writing – original draft, Supervision, Resources, Methodology, Formal analysis. **Mónica Cicuéndez:** Investigation, Formal analysis. **Daniela M. da Silva:** Investigation, Formal analysis. **Nathalie Barroca:** Writing – original draft, Visualization, Methodology, Investigation, Formal analysis. **Francisco-Javier Fernández-San-Argimiro:** Investigation, Formal analysis. **Iratxe Madarieta:** Writing – review & editing. **Laura Casarrubios:** Investigation, Formal analysis. **María José Feito:** Investigation, Formal analysis. **Rosalía Diez-Orejas:** Investigation, Formal analysis. **Rita Ferreira:** Writing – original draft, Investigation, Formal analysis. **Sander C.G. Leeuwenburgh:** Writing – review & editing, Supervision. **María Teresa Portolés:** Writing – review & editing, Supervision, Resources, Project administration, Funding acquisition, Conceptualization. **Paula A.A.P. Marques:** Writing – review & editing, Supervision, Resources, Project administration, Funding acquisition, Conceptualization. **X. Frank Walboomers:** Writing – review & editing, Supervision, Resources, Project administration, Funding acquisition, Conceptualization.

Declaration of competing interest

The authors declare that they have no known competing financial interests or personal relationships that could have appeared to influence the work reported in this paper.

Data availability

Data will be made available on request.

Acknowledgements

This work was supported by the European Union's Horizon 2020 research and innovation programme under grant agreement No 829060. The authors would like to thank Nerea Garcia-Urkia, Olatz Murua, Beatriz Olalde and the colleagues of TECNALIA for their work on the decellularization of adipose tissue to obtain the adECM material, as well as for the circular dichroism analysis, mechanical characterization and scaffolding. Furthermore, the authors would like to acknowledge the work of Maikel M.A. School, who assisted in performing animal surgery and post-operative care, and Natasja W.M. van Dijk and René van Rheden, for their help during tissue processing and immunohistochemical analysis. Furthermore, the authors would like to express their appreciation to Professor Piet Slootweg, for the valuable histopathological screening of all tissue sections, and to the colleagues of

NeuroStimSpinal for their active contribution during scientific discussion of the present work.

List of abbreviations

SCI	spinal cord injury
ECM	extracellular matrix
adECM	adipose tissue-derived extracellular matrix
rGO	reduced graphene oxide
GBMs	graphene-based materials
XPS	X-ray photoelectron spectroscopy
SEM	scanning electron microscopy
μCT	X-ray microtomography
CCK-8	cell counting kit-8
CLSM	confocal laser scanning microscopy
H&E	hematoxylin and eosin
FBGCs	foreign body giant cells
FBR	foreign body reaction/response
CD80/86/163/206	cluster of differentiation 80/86/163/206
TP	total protein
CHOL	cholesterol
TG	triglycerides
Glc	glucose
ALB	albumin
ALP	alkaline phosphatase
ALAT	alanine aminotransferase
ASAT	aspartate aminotransferase
GGT	gamma-glutamyltransferase
CK-MB	creatine kinase-myocardial band
CREAT	creatinine

Appendix A. Supplementary data

Supplementary data to this article can be found online at https://doi.org/10.1016/j.mtbio.2024.101059.

References

[1] C.S. Ahuja, J.R. Wilson, S. Nori, M.R.N. Kotter, C. Druschel, A. Curt, M.G. Fehlings, Traumatic spinal cord injury, Nat. Rev. Dis. Prim. 3 (2017) 17018, https://doi.org/10.1038/nrdp.2017.18.

[2] T. Führmann, P.N. Anandakumaran, M.S. Shoichet, Combinatorial Therapies after spinal cord injury: how can biomaterials help? Adv. Healthcare Mater. 6 (10) (2017) https://doi.org/10.1002/adhm.201601130, 10.1002/adhm.201601130.

[3] H. Shen, B. Xu, C. Yang, W. Xue, Z. You, X. Wu, D. Ma, D. Shao, K. Leong, J. Dai, A DAMP-scavenging, IL-10-releasing hydrogel promotes neural regeneration and motor function recovery after spinal cord injury, Biomaterials 280 (2022) 121279, https://doi.org/10.1016/j.biomaterials.2021.121279.

[4] X. Gao, Z. You, Y. Li, X. Kang, W. Yang, H. Wang, T. Zhang, X. Zhao, Y. Sun, H. Shen, J. Dai, Multifunctional hydrogel modulates the immune microenvironment to improve allogeneic spinal cord tissue survival for complete spinal cord injury repair, Acta Biomater. 155 (2023) 235–246, https://doi.org/10.1016/j.actbio.2022.11.015.

[5] R. Zhu, X. Zhu, Y. Zhu, Z. Wang, X. He, Z. Wu, L. Xue, W. Fan, R. Huang, Z. Xu, X. Qi, W. Xu, Y. Yu, Y. Ren, C. Li, Q. Cheng, L. Ling, S. Wang, L. Cheng, Immunomodulatory layered Double hydroxide nanoparticles enable neurogenesis by targeting transforming growth factor-β receptor 2, ACS Nano 15 (2) (2021) 2812–2830, https://doi.org/10.1021/acsnano.0c08727.

[6] P. Chen, C. Xu, P. Wu, K. Liu, F. Chen, Y. Chen, H. Dai, Z. Luo, Wirelessly powered electrical-stimulation based on biodegradable 3D piezoelectric scaffolds promotes the spinal cord injury repair, ACS Nano 16 (10) (2022) 16513–16528, https://doi.org/10.1021/acsnano.2c05818.

[7] A.F. Girão, M.C. Serrano, A. Completo, P.A.A.P. Marques, Is graphene shortening the path toward spinal cord regeneration? ACS Nano 16 (9) (2022) 13430–13467, https://doi.org/10.1021/acsnano.2c04756.

[8] X. Zhang, X. Chen, H. Hong, R. Hu, J. Liu, C. Liu, Decellularized extracellular matrix scaffolds: recent trends and emerging strategies in tissue engineering, Bioact. Mater. 10 (2021) 15–31, https://doi.org/10.1016/j.bioactmat.2021.09.014.

[9] J.M. Fishman, K. Wiles, K.J. Wood, in: Host Response Biomater, Academic Press, Oxford, UK, 2015, pp. 151–187.

[10] A.E. Haggerty, I. Maldonado-Lasunción, M. Oudega, Biomaterials for revascularization and immunomodulation after spinal cord injury, Biomed. Mater. 13 (4) (2018) 044105, https://doi.org/10.1088/1748-605X/aaa9d8.

[11] A. Guijarro-Belmar, A. Varone, M.R. Baltzer, S. Kataria, E. Tanriver-Ayder, R. Watzlawick, E. Sena, C.J. Cunningham, A.M. Rajnicek, M. Macleod, W. Huang, G.L. Currie, S.K. McCann, Effectiveness of biomaterial-based combination strategies for spinal cord repair - a systematic review and meta-analysis of preclinical literature, Spinal Cord 60 (12) (2022) 1041–1049, https://doi.org/10.1038/s41393-022-00811-z.

[12] M. Cicuéndez, L. Casarrubios, M.J. Feito, I. Madarieta, N. Garcia-Urkia, O. Murua, B. Olalde, N. Briz, R. Diez-Orejas, M.T. Portolés, Effects of human and porcine adipose extracellular matrices decellularized by enzymatic or chemical methods on macrophage polarization and immunocompetence, Int. J. Mol. Sci. 22 (8) (2021) 3847, https://doi.org/10.3390/ijms22083847.

[13] L. Daneshmandi, M. Barajaa, A. Tahmasbi Rad, S.A. Sydlik, C.T. Laurencin, Graphene-based biomaterials for bone regenerative engineering: a comprehensive review of the field and considerations regarding biocompatibility and biodegradation, Adv. Healthcare Mater. 10 (1) (2021) e2001414, https://doi.org/10.1002/adhm.202001414.

[14] O. Akhavan, Graphene scaffolds in progressive nanotechnology/stem cell-based tissue engineering of the nervous system, J. Mater. Chem. B 4 (19) (2016) 3169–3190, https://doi.org/10.1039/c6tb00152a.

[15] W. Guo, X. Zhang, X. Yu, S. Wang, J. Qiu, W. Tang, L. Li, H. Liu, Z.L. Wang, Self-powered electrical stimulation for enhancing neural differentiation of mesenchymal stem cells on graphene-poly(3,4-ethylenedioxythiophene) hybrid microfibers, ACS Nano 10 (5) (2016) 5086–5095, https://doi.org/10.1021/acsnano.6b00200.

[16] A Polo-Montalvo, M Cicuéndez, L Casarrubios, N Barroca, D da Silva, MJ Feito, R Diez-Orejas, MC Serrano, PAAP Marques, MT Portolés, Effects of graphene oxide and reduced graphene oxide nanomaterials on porcine endothelial progenitor cells, Nanoscale 15 (42) (2023) 17173–17183, https://doi.org/10.1039/d3nr03145d. PMID: 37853851.

[17] J. Park, Y.S. Kim, S. Ryu, W.S. Kang, S. Park, J. Han, H.C. Jeong, B.H. Hong, Y. Ahn, B.-S. Kim, Graphene potentiates the myocardial repair efficacy of mesenchymal stem cells by stimulating the expression of angiogenic growth factors and gap junction protein, Adv. Funct. Mater. 25 (2015) 2590–2600, https://doi.org/10.1002/adfm.201500365.

[18] M.C. Serrano, J. Patiño, C. García-Rama, M.L. Ferrer, J.L.G. Fierro, A. Tamayo, J. E. Collazos-Castro, F. del Monte, M.C. Gutiérrez, 3D free-standing porous scaffolds made of graphene oxide as substrates for neural cell growth, J. Mater. Chem. B 2 (34) (2014) 5698–5706, https://doi.org/10.1039/C4TB00652F.

[19] A. Domínguez-Bajo, A. González-Mayorga, C.R. Guerrero, F.J. Palomares, R. García, E. López-Dolado, M.C. Serrano, Myelinated axons and functional blood vessels populate mechanically compliant rGO foams in chronic cervical hemisected rats, Biomaterials 192 (2019) 461–474, https://doi.org/10.1016/j.biomaterials.2018.11.024.

[20] N. Barroca, D.M. da Silva, S.C. Pinto, J.P.M. Sousa, K. Verstappen, A. Klymov, F. J. Fernández-San-Argimiro, I. Madarieta, O. Murua, B. Olalde, L. Papadimitriou, K. Karali, K. Mylonaki, E. Stratakis, A. Ranella, P.A.A.P. Marques, Interfacing reduced graphene oxide with an adipose-derived extracellular matrix as a regulating milieu for neural tissue engineering, Biomater. Adv. 148 (2023) 213351, https://doi.org/10.1016/j.bioadv.2023.213351.

[21] T. Hu, C.J. Brinker, W.C.W. Chan, C. Chen, X. Chen, D. Ho, K. Kataoka, N.A. Kotov, L.M. Liz-Marzán, A.E. Nel, W.J. Parak, M. Stevens, Publishing translational research of nanomedicine in ACS nano, ACS Nano 16 (11) (2022) 17479–17481, https://doi.org/10.1021/acsnano.2c10967.

[22] J.M. Anderson, A. Rodriguez, D.T. Chang, Foreign body reaction to biomaterials, Semin. Immunol. 20 (2) (2008) 86–100, https://doi.org/10.1016/j.smim.2007.11.004.

[23] Z. Sheikh, P.J. Brooks, O. Barzilay, N. Fine, M. Glogauer, Macrophages, foreign body giant cells and their response to implantable biomaterials, Materials 8 (9) (2015) 5671–5701, https://doi.org/10.3390/ma8095269.

[24] M. Kasravi, A. Ahmadi, A. Babajani, R. Mazloomnejad, M.R. Hatamnejad, S. Shariatzadeh, S. Bahrami, H. Niknejad, Immunogenicity of decellularized extracellular matrix scaffolds: a bottleneck in tissue engineering and regenerative medicine, Biomater. Res. 27 (1) (2023) 10, https://doi.org/10.1186/s40824-023-00348-z.

[25] J. Ma, R. Liu, X. Wang, Q. Liu, Y. Chen, R.P. Valle, Y.Y. Zuo, T. Xia, S. Liu, Crucial role of lateral size for graphene oxide in activating macrophages and stimulating pro-inflammatory responses in cells and animals, ACS Nano 9 (10) (2015) 10498–10515, https://doi.org/10.1021/acsnano.5b04751.

[26] Y.C. Cho, P.J. Pak, Y.H. Joo, H.S. Lee, N. Chung, In vitro and in vivo comparison of the immunotoxicity of single- and multi-layered graphene oxides with or without pluronic F-127, Sci. Rep. 6 (2016) 38884, https://doi.org/10.1038/srep38884.

[27] M. Xu, J. Zhu, F. Wang, Y. Xiong, Y. Wu, Q. Wang, J. Weng, Z. Zhang, W. Chen, S. Liu, Improved in vitro and in vivo biocompatibility of graphene oxide through surface modification: poly(acrylic acid)-functionalization is superior to PEGylation, ACS Nano 10 (3) (2016) 3267–3281, https://doi.org/10.1021/acsnano.6b00539.

[28] M. Cicuéndez, L. Casarrubios, N. Barroca, D. Silva, M.J. Feito, R. Diez-Orejas, P.A. A.P. Marques, M.T. Portolés, Benefits in the macrophage response due to graphene oxide reduction by thermal treatment, Int. J. Mol. Sci. 22 (13) (2021) 6701, https://doi.org/10.3390/ijms22136701.

[29] S.A. Sydlik, S. Jhunjhunwala, M.J. Webber, D.G. Anderson, R. Langer, In vivo compatibility of graphene oxide with differing oxidation states, ACS Nano 9 (4) (2015) 3866–3874, https://doi.org/10.1021/acsnano.5b01290.

[30] J.-H. Liu, T. Wang, H. Wang, Y. Gu, Y. Xu, H. Tang, G. Jia, Y. Liu, Biocompatibility of graphene oxide intravenously administrated in mice—effects of dose, size and exposure protocols, Toxicol. Res. 4 (1) (2015) 83–91, https://doi.org/10.1039/c4tx00044g.

[31] X. Zhang, J. Yin, C. Peng, W. Hu, Z. Zhu, W. Li, C. Fan, Q. Huang, Distribution and biocompatibility studies of graphene oxide in mice after intravenous administration, Carbon 49 (3) (2011) 986–995, https://doi.org/10.1016/j.carbon.2010.11.005.
[32] H. Tang, J.F.A. Husch, Y. Zhang, J.A. Jansen, F. Yang, J.J.J.P. van den Beucken, Coculture with monocytes/macrophages modulates osteogenic differentiation of adipose-derived mesenchymal stromal cells on poly(lactic-co-glycolic) acid/polycaprolactone scaffolds, J. Tissue Eng. Regen. Med. 13 (5) (2019) 785–798, https://doi.org/10.1002/term.2826.
[33] E.J. Speel, M.P. Jansen, F.C. Ramaekers, A.H. Hopman, A novel triple-color detection procedure for brightfield microscopy, combining in situ hybridization with immunocytochemistry, J. Histochem. Cytochem. 42 (10) (1994) 1299–1307, https://doi.org/10.1177/42.10.7930513.
[34] A. Lipatov, M.J.-F. Guinel, D.S. Muratov, V.O. Vanyushin, P.M. Wilson, A. Kolmakov, A. Sinitskii, Low-temperature thermal reduction of graphene oxide: in situ correlative structural, thermal desorption, and electrical transport measurements, Appl. Phys. Lett. 112 (5) (2018) 053103, https://doi.org/10.1063/1.4996337.
[35] A.F. Girão, J. Sousa, A. Domínguez-Bajo, A. González-Mayorga, I. Bdikin, E. Pujades-Otero, N. Casañ-Pastor, M.J. Hortigüela, G. Otero-Irurueta, A. Completo, M.C. Serrano, P.A.A.P. Marques, 3D reduced graphene oxide scaffolds with a combinatorial fibrous-porous architecture for neural tissue engineering, ACS Appl. Mater. Interfaces 12 (35) (2020) 38962–38975, https://doi.org/10.1021/acsami.0c10599.
[36] K.L. Scott, D.C. Dunand, Freeze casting – a review of processing, microstructure and properties via the open data repository, FreezeCasting.net, Prog. Mater. Sci. 94 (2018) 243–305, https://doi.org/10.1016/j.pmatsci.2018.01.001.
[37] C.M. Murphy, F.J. O'Brien, Understanding the effect of mean pore size on cell activity in collagen-glycosaminoglycan scaffolds, Cell Adh. Migr. 4 (3) (2010) 377–381, https://doi.org/10.4161/cam.4.3.11747.
[38] E. Moeendarbary, I.P. Weber, G.K. Sheridan, D.E. Koser, S. Soleman, B. Haenzi, E. J. Bradbury, J. Fawcett, K. Franze, The soft mechanical signature of glial scars in the central nervous system, Nat. Commun. 8 (2017) 14787, https://doi.org/10.1038/ncomms14787.
[39] K.M. Pawelec, A. Husmann, S.M. Best, R.E. Cameron, Understanding anisotropy and architecture in ice-templated biopolymer scaffolds, Mater. Sci. Eng. C 37 (2014) 141–147, https://doi.org/10.1016/j.msec.2014.01.009.
[40] H. Joukhdar, A. Seifert, T. Jüngst, J. Groll, M.S. Lord, J. Rnjak-Kovacina, Ice templating soft matter: fundamental principles and fabrication approaches to tailor pore structure and morphology and their biomedical applications, Adv. Mater. 33 (34) (2021) 2100091.
[41] J.A. Cyr, A. Husmann, S.M. Best, R.E. Cameron, Complex architectural control of ice-templated collagen scaffolds using a predictive model, Acta Biomater. 153 (2022) 260–272, https://doi.org/10.1016/j.actbio.2022.09.034.
[42] T.A. Wynn, K.M. Vannella, Macrophages in tissue repair, regeneration, and fibrosis, Immunity 44 (3) (2016) 450–462, https://doi.org/10.1016/j.immuni.2016.02.015.
[43] N. Parameswaran, S. Patial, Tumor necrosis factor-α signaling in macrophages, Crit. Rev. Eukaryot. Gene Expr. 20 (2) (2010) 87–103, https://doi.org/10.1615/critreveukargeneexpr.v20.i2.10.
[44] M. Rothaug, C. Becker-Pauly, S. Rose-John, The role of interleukin-6 signaling in nervous tissue, Biochim. Biophys. Acta 1863 (6 Pt A) (2016) 1218–1227, https://doi.org/10.1016/j.bbamcr.2016.03.018.
[45] M.J. Feito, M. Cicuéndez, L. Casarrubios, R. Diez-Orejas, S. Fateixa, D. Silva, N. Barroca, P.A.A.P. Marques, M.T. Portolés, Effects of graphene oxide and reduced graphene oxide nanostructures on CD4+ Th2 lymphocytes, Int. J. Mol. Sci. 23 (18) (2022) 10625, https://doi.org/10.3390/ijms231810625.
[46] K. Verstappen, R. Aquarius, A. Klymov, K.E. Wever, L. Damveld, S.C. G. Leeuwenburgh, R.H.M.A. Bartels, C.R. Hooijmans, X.F. Walboomers, Systematic evaluation of spinal cord injury animal models in the field of biomaterials, Tissue Eng., Part B 28 (6) (2022) 1169–1179, https://doi.org/10.1089/ten.TEB.2021.0194.
[47] Y.S. Gwak, B.C. Hains, K.M. Johnson, C.E. Hulsebosch, Effect of age at time of spinal cord injury on behavioral outcomes in rat, J. Neurotrauma 21 (8) (2004) 983–993, https://doi.org/10.1089/0897715041650999.
[48] J.A. Clark Jr., P.H. Myers, M.F. Goelz, J.E. Thigpen, D.B. Forsythe, Pica behavior associated with buprenorphine administration in the rat, Lab. Anim. Sci. 47 (3) (1997) 300–303.
[49] V.S. Harikrishnan, L.K. Krishnan, K.S.P. Abelson, A novel technique to develop thoracic spinal laminectomy and a methodology to assess the functionality and welfare of the contusion spinal cord injury (SCI) rat model, PLoS One 14 (7) (2019) e0219001, https://doi.org/10.1371/journal.pone.0219001.
[50] A. Carnicer-Lombarte, S.T. Chen, G.G. Malliaras, D.G. Barone, Foreign body reaction to implanted biomaterials and its impact in nerve neuroprosthetics, Front. Bioeng. Biotechnol. 9 (2021) 622524, https://doi.org/10.3389/fbioe.2021.622524.
[51] S. Liu, C. Zhou, S. Mou, J. Li, M. Zhou, Y. Zeng, C. Luo, J. Sun, Z. Wang, W. Xu, Biocompatible graphene oxide-collagen composite aerogel for enhanced stiffness and in situ bone regeneration, Mater. Sci. Eng. C 105 (2019) 110137, https://doi.org/10.1016/j.msec.2019.110137.
[52] L. Li, Y. Liang, G. Wang, P. Xu, L. Yang, S. Hou, J. Zhou, L. Wang, X. Li, L. Yang, Y. Fan, In vivo disintegration and bioresorption of a nacre-inspired graphene-silk film caused by the foreign-body reaction, iScience 23 (6) (2020) 101155, https://doi.org/10.1016/j.isci.2020.101155.
[53] R. Milde, J. Ritter, G.A. Tennent, A. Loesch, F.O. Martinez, S. Gordon, M.B. Pepys, A. Verschoor, L. Helming, Multinucleated giant cells are specialized for complement-mediated phagocytosis and large target destruction, Cell Rep. 13 (9) (2015) 1937–1948, https://doi.org/10.1016/j.celrep.2015.10.065.
[54] B. Ten Harkel, J. Koopsen, S.M. van Putten, H. van Veen, D.I. Picavet, T.J. de Vries, R.A. Bank, V. Everts, Ultrastructural aspects of foreign body giant cells generated on different substrates, J. Struct. Biol. 195 (1) (2016) 31–40, https://doi.org/10.1016/j.jsb.2016.04.016.
[55] S.P. Mukherjee, A.R. Gliga, B. Lazzaretto, B. Brandner, M. Fielden, C. Vogt, L. Newman, A.F. Rodrigues, W. Shao, P.M. Fournier, M.S. Toprak, A. Star, K. Kostarelos, K. Bhattacharya, B. Fadeel, Graphene oxide is degraded by neutrophils and the degradation products are non-genotoxic, Nanoscale 10 (3) (2018) 1180–1188, https://doi.org/10.1039/c7nr03552g.
[56] B. Ten Harkel, T. Schoenmaker, D.I. Picavet, N.L. Davison, T.J. de Vries, V. Everts, The foreign body giant cell cannot resorb bone, but dissolves hydroxyapatite like osteoclasts, PLoS One 10 (10) (2015) e0139564, https://doi.org/10.1371/journal.pone.0139564.
[57] S. Al-Maawi, A. Orlowska, R. Sader, C. James Kirkpatrick, S. Ghanaati, In vivo cellular reactions to different biomaterials-Physiological and pathological aspects and their consequences, Semin. Immunol. 29 (2017) 49–61, https://doi.org/10.1016/j.smim.2017.06.001.
[58] B.N. Brown, R. Londono, S. Tottey, L. Zhang, K.A. Kukla, M.T. Wolf, K.A. Daly, J. E. Reing, S.F. Badylak, Macrophage phenotype as a predictor of constructive remodeling following the implantation of biologically derived surgical mesh materials, Acta Biomater. 8 (3) (2012) 978–987, https://doi.org/10.1016/j.actbio.2011.11.031.
[59] L.R. Madden, D.J. Mortisen, E.M. Sussman, S.K. Dupras, J.A. Fugate, J.L. Cuy, K. D. Hauch, M.A. Laflamme, C.E. Murry, B.D. Ratner, Proangiogenic scaffolds as functional templates for cardiac tissue engineering, Proc. Natl. Acad. Sci. U S A 107 (34) (2010) 15211–15216, https://doi.org/10.1073/pnas.1006442107.
[60] R. Sridharan, A.R. Cameron, D.J. Kelly, C.J. Kearney, F.J. O'Brien, Biomaterial based modulation of macrophage polarization: a review and suggested design principles, Mater. Today 18 (6) (2015) 313–325.
[61] A.K. McNally, J.M. Anderson, Foreign body-type multinucleated giant cells induced by interleukin-4 express select lymphocyte co-stimulatory molecules and are phenotypically distinct from osteoclasts and dendritic cells, Exp. Mol. Pathol. 91 (3) (2011) 673–681, https://doi.org/10.1016/j.yexmp.2011.06.012.
[62] Y. Chandorkar, R. K, B. Basu, The foreign body response demystified, ACS Biomater. Sci. Eng. 5 (1) (2019) 19–44, https://doi.org/10.1021/acsbiomaterials.8b00252.
[63] R.T. Hannan, S.M. Peirce, T.H. Barker, Fibroblasts: diverse cells critical to biomaterials integration, ACS Biomater. Sci. Eng. 4 (4) (2018) 1223–1232, https://doi.org/10.1021/acsbiomaterials.7b00244.
[64] L.M. Delgado, Y. Bayon, A. Pandit, D.I. Zeugolis, To cross-link or not to cross-link? Cross-linking associated foreign body response of collagen-based devices, Tissue Eng. B Rev. 21 (3) (2015) 298–313, https://doi.org/10.1089/ten.TEB.2014.0290.
[65] L. Ou, B. Song, H. Liang, J. Liu, X. Feng, B. Deng, T. Sun, L. Shao, Toxicity of graphene-family nanoparticles: a general review of the origins and mechanisms, Part. Fibre Toxicol. 13 (1) (2016) 57, https://doi.org/10.1186/s12989-016-0168-y.
[66] J. Zaias, M. Mineau, C. Cray, D. Yoon, N.H. Altman, Reference values for serum proteins of common laboratory rodent strains, J. Am. Assoc. Lab. Anim. Sci. 48 (4) (2009) 387–390.
[67] E. López-Dolado, A. González-Mayorga, M.C. Gutiérrez, M.C. Serrano, Immunomodulatory and angiogenic responses induced by graphene oxide scaffolds in chronic spinal hemisected rats, Biomaterials 99 (2016) 72–81, https://doi.org/10.1016/j.biomaterials.2016.05.012.
[68] K. Wang, J. Ruan, H. Song, J. Zhang, Y. Wo, S. Guo, D. Cui, Biocompatibility of graphene oxide, Nanoscale Res. Lett. 6 (1) (2011) 8, https://doi.org/10.1007/s11671-010-9751-6.
[69] S. Syama, W. Paul, A. Sabareeswaran, P.V. Mohanan, Raman spectroscopy for the detection of organ distribution and clearance of PEGylated reduced graphene oxide and biological consequences, Biomaterials 131 (2017) 121–130, https://doi.org/10.1016/j.biomaterials.2017.03.043.